A satellite-derived database for stand-replacing windthrow events in boreal forests of European Russia in 1986–2017

Andrey N. Shikhov[1], Alexander V. Chernokulsky[2], Igor O. Azhigov[1] and Anastasia V. Semakina[1]

[1]Perm State University, Perm, 614990, Russia
[2]A.M. Obukhov Institute of Atmospheric Physics, Russian Academy of Sciences, Moscow, 119017, Russia

Correspondence to: Andrey N. Shikhov (shikhovan@gmail.com)

Abstract. Severe winds are among the main causes of disturbances in boreal and temperate forests. Here, we present a new GIS database of stand-replacing windthrow events in the forest zone of European Russia (ER) for the 1986–2017 period. Delineation of windthrow areas was based on the full Landsat archive and two Landsat-derived products on forest cover change, namely the Global Forest Change and the Eastern' Europe Forest Cover Change datasets. Subsequent verification and analysis of each windthrow was carried out manually to determine the type of related storm event, its date or date range, and geometrical characteristics. The database contains 102,747 elementary areas of damaged forest that were combined into 700 windthrow events caused by 486 convective or non-convective storms. The database includes stand-replacing windthrow only, with an area > 0.05 km^2 and > 0.25 km^2 for the events caused by tornadoes and other storms, respectively. Additional information such as weather station reports and event description from media sources is also provided. The total area of stand-replacing windthrow amounts to 2966 km^2, that is 0.19% of the forested area of the study region. Convective windstorms contribute 82.5% to the total wind-damaged area, while tornadoes and non-convective windstorms are responsible for 12.9% and 4.6% of this area, respectively. Most of windthrow events in the ER happened in summer, which is in contrast to Western and Central Europe, where they mainly occur in autumn and winter. Due to several data and method limitations, the compiled database is spatially and temporally inhomogeneous and hence incomplete. Despite this incompleteness, the presented database provides a valuable source of spatial and temporal information on windthrow in the ER and can be used by both science and management. The database is available at https://doi.org/10.6084/m9.figshare.12073278.v6 (Shikhov et al., 2020).

1 Introduction

Forests are a valuable natural resource that is important for economy, society and sustainable development. Forest ecosystems are regularly exposed to natural disturbance agents such as fires, droughts, insect outbreaks, or windstorms. Being an intrinsic part of forest ecosystem dynamics (Attiwill, 1994; Seidl et al., 2017), natural disturbances cause substantial environmental and economic damage (Schelhaas et al., 2003; Gardiner et al., 2010; van Lierop et al., 2015). In boreal and temperate forests, windstorms constitute one of the main drivers of natural disturbances (Ulanova, 2000; Forzieri et al., 2020). In Europe, windthrow contribute more than a half to the total area of natural disturbances, including abiotic and biotic causes (Schelhaas, 2003; Gardiner et al., 2010).

Recently, disturbance regimes have changed considerably in many forest ecosystems worldwide (Seidl et al., 2011, 2017; Senf et al., 2018). Particularly, both the occurrence and severity of disturbance has increased in different regions, including those related to forest fires (Westerling, 2016; Kukavskaya et al., 2016), insect outbreaks (Kautz et al., 2017), and droughts (Millar et al., 2015). Researchers have revealed a statistically significant increase of wind-related forest disturbance in Western, Central, and Northern Europe (Seidl et al., 2014; Gregow et al., 2017), and in European Russia (Potapov et al., 2015).

The observed increase in the frequency and severity of windthrow events is associated with changes in forest structure like increasing growing stock and median age, primarily in coniferous forests (Schelhaas et al., 2003; Senf et al., 2018), and with climatic changes (Overpeck et al., 1990; Lassig and Moĉalov, 2000; Seidl et al., 2011; 2014; 2017). An intensification of winter windstorms (Gardiner et al., 2010; Usbeck et al., 2010; Gregow et al., 2017) and an increase in the frequency and intensity of severe convective storms in the warm season (Overpeck et al., 1994; Diffenbaugh et al., 2013; Chernokulsky et al., 2017; Radler et al., 2019) can be considered as the main climatic drivers for increasing wind-related damage in boreal and temperate forests.

For correct attribution of forest windthrow to particular causes, it is important to obtain corresponding data on such events. Recently, several long-term databases of windthrow events in boreal and temperate forests, often together with other types of disturbances, have been collected at a national and international scale. The longest windthrow data series have been compiled in Sweden (Nilsson et al., 2003) and Switzerland (Usbeck et al., 2010) based on literature reviews and forestry services reports. European Forest Institute compiled the database of destructive storms in European forests for 1951−2010 (Gardiner et al., 2010). A new GIS database of wind disturbance in European forests has been compiled in 2019 by aggregating multiple datasets collected by 26 research institutes and forestry services across Europe (Forzieri et al, 2020). It comprises more than 80.000 forest areas that were disturbed by wind in 2000-2018. Compare to other European countries, windthrow events in Russia remain understudied. Long-term databases of windthrow events have been collected only for individual regions, for example, for the Middle Ural (Lassig and Moĉalov, 2000) and the Central Forest Reserve in the Tver region (Ulanova, 2000).

The main data sources of previously compiled windthrow databases in Russia were the literature reviews, reports of forestry services, aerial observations and field investigations (Skvortsova et al., 1983; Lassig and Moĉalov, 2000; Ulanova, 2000). Meanwhile, satellite images have become the important data source for windthrow monitoring in Russian forests in recent decades (Krylov et al., 2012). Indeed, satellite data can be especially informative for studying Russian low-populated boreal forests, known in Russia as the taiga, which represent the largest forested region globally. They cover approximately 7.63 million km^2, which is 22% of the world's forest areas (WWF Russia's boreal forests, 2007).

Use of satellite images for obtaining information on windthrow was proposed back in 1975 (Sayn-Wittgenstein and Wightman, 1975). However, the widespread utilising of satellite data to estimate the inter-annual variability of wind-related forest damage (e.g. Fraser et al., 2005; Baumann et al., 2014) became feasible after the opening of Landsat archive (Wulder et al., 2012), and two Landsat-based products, namely the Global Forest Change (GFC) map (Hansen et al., 2013) and the Eastern' Europe Forest Cover Change (EEFCC) (Potapov et al., 2015). Thus, GIS databases of windthrow events have been collected for some Russian regions based on Landsat archive and GFC data, i.e., for the Ural and north-eastern part of the ER (Shikhov and Zaripov, 2018; Shikhov et al., 2019), Kostroma region and adjacent areas (Petukhov and Nemchinova, 2014), and South Sakhalin (Korznikov et al., 2019). Shikhov and Chernokulsky (2018) found 110 previously unknown tornado-induced windthrow areas in ER based on satellite images. However, for the entire ER, there are only rough estimates of storm-related forest damage (Potapov et al., 2015). The contribution of various weather phenomena like convective and non-convective windstorms, snowstorms, or tornadoes to the total wind-induced forest damage, as well as interannual and seasonal distribution of windthrow events remains unknown for the ER territory. The appearance of such data can be helpful for forest science and management as well as for severe storms investigations.

In this study, we present a detailed GIS database of relatively large stand-replacing windthrow events in the forest zone of the ER for the period 1986-2017. The database contains windthrow areas with indication of storm event types and dates, geometrical characteristics of windthrow areas, and additional information. To determine these characteristics, we use the Landsat archive, the GFC and EEFCC Landsat-based forest loss data products, high-resolution satellite images from public map services, supplementary information including weather stations observations, databases on hazardous weather events, damage reports in the media sources, and reanalysis data. We describe the used data and the study region in Section 2, and explain the database structure in Section 3. Section 4 describes the windthrow delineation process and assessment of the geometrical parameters of windthrow areas. Section 5 presents spatio-temporal variability of wind-damaged areas and distributions of their geometrical characteristics. Section 6 discusses the main limitations of the method and the compiled dataset, while Section 6 draws the main conclusions of the paper.

2 Region and data

2.1 The study region

The study region includes the forest zone of the ER (Fig. 1) between the forest-steppe transition zone on the south and forest-tundra transition zone on the north. The availability of the EEFCC dataset determines the eastern boundary of the study region that broadly coincides with the Ural Ridge.

We used the 250-m resolution map of the vegetation cover of Russia (Bartalev et al., 2016) to estimate forest-covered area and dominant forest species (Fig. 1). Forests cover 54.6% of the study region. The most widespread dominant forest species are dark-coniferous (*Picea abies, Picea obovata, Ábies sibírica*), light-coniferous (*Pinus sylvestris*), small-leaved (*Betula pendula, Betula pubescens, Pópulus trémula*) and some broadleaved species (*Tília cordáta, Quercus robur et al.*) (Kalyakin et al., 2004). Secondary (re-grown after logging or wildfires) small-leaved and mixed forests cover approximately 61% of the total forested area. Old-growth dark-coniferous forests are widespread on the western slope of the Northern Ural and the adjacent plain, and pine forests cover the largest area (>100 thousand km^2) on the northwest of the ER (Fig. 1).

2.2 Initial data

We used multiple data sources to collect information on windthrow events for the 1986-2017 period. Particularly, we utilized satellite data to delineate windthrow areas and determine a storm event type and used additional information to determine the dates of storm events.

Primary information for windthrow delineation and verification The Landsat-based GFC data were utilised to search and delineate forest areas affected by storm events in 2001–2017. The data come as the integer raster with a 30 m cell size. It contains information on stand-replacing forest disturbances at annual temporal resolution. In the boreal forest regions, the overall accuracy of the forest loss detection in the GFC is 99.3%, while user's and producer's accuracies are 93.9% and 88.0%, respectively (Hansen et al., 2013). Here, producer's accuracy is the ratio of correctly classified forest loss area to the actual forest loss area; user's accuracy is the ratio of correctly classified forest loss area to the same area according to the verified forest loss area. The GFC data were downloaded from http://earthenginepartners.appspot.com/google.com/gMG7KbLG. The EEFCC dataset was used to search and delineate windthrow areas in 1986–2000. The data come as the integer raster with a 30 m cell size. It contains information on forest loss classified into four broad periods: 1986–1988, 1989–2000, 2001–2006 and 2007–2012. This rough time determination is associated with rareness of the Landsat images between 1989 and 1998. The detection of gross forest loss in the EEFCC has producer's and user's accuracy of 88% and 89%, respectively (Potapov et al., 2015). The data were downloaded from https://glad.geog.umd.edu/dataset/eastern-europe-forset-cover-dynamics-1985-2012/.

Landsat images (L1T processing level), i.e., images from the Landsat Thematic Mapper (TM), the Enhanced Thematic Mapper Plus (ETM+), and the Operational Land Imager (OLI), were used to confirm the wind-related nature of forest disturbance, determine the storm types, dates (or ranges of dates) of windthrow occurrence in 1986–2017. It addition, many windthrow areas appeared before 2001 were delineated with Landsat images (see Section 3.1.3 for details). Sentinel-2 images were used to confirm the wind-related nature of forest disturbance, determine the storm types, dates (or ranges of

dates) of windthrow events occurrence for the 2016–2017 period. We downloaded the Landsat and Sentinel-2 images from https://earthexplorer.usgs.gov/ and https://eos.com/landviewer.

High-resolution (0.5–2 m) satellite images, hereinafter HRI, were used to discriminate the type of a storm event, causing windthrow (windstorm or tornado). Usually 2–8 high-resolution images are available for the period 2001–2017. No HRI are available before 2001. To view and analyze the HRI, we used mainly Google Earth Pro, while other public map services (i.e., Bing Maps, ESRI Imagery, Here) were used to a lesser degree. We should highlight that the availability of the HRI substantially vary among different parts of the ER. In particular, some areas in the northern part of the ER are not covered by the HRI.

Additional information on storm events

Information of 3-hourly weather reports was used to determine storm event dates, and match the reported wind gusts, if any, with windthrow events. We utilized information on observed wind speed, precipitation, hail and thunderstorm occurrence. The routine meteorological observations have been collected at 402 meteorological stations located within the studied area and have been initially processed at the All-Russian Research Institute of Hydrometeorological Information—World Data Center (RIHMI-WDC) from 1966 to the present (Bulygina et al., 2014). Monthly reviews of hazardous weather events occurred in Russia, which are published in the Russian Meteorology and Hydrology journal (http://mig-journal.ru/en/archive-eng) but not translated, were also used to determine storm event dates for the 2001–2017 period. Additionally, these reviews contain the descriptions of hazardous weather events and damage reports. We included this information into our database. The RIHMI-WDC database of hazardous weather events (Shamin et al., 2019) and information from regional departments of the Russian state weather service were also utilized to determine the dates of several storms that caused windthrow events in 1986–2017. Media news and witness reports in social networks, including photos and videos, were used for obtaining additional information on the type of event, i.e., tornadic or non-tornadic, for the 1986–2017 period. Data from meteorological satellites Terra/Aqua MODIS (from 2001) and Meteosat-8 (from 2016) were used for obtaining additional information on storm events causing windthrow, especially to determine storm date and time. In particular, the Collection 6 MODIS Active Fire data (Giglio et al., 2016) were used to discriminate fire- and wind-related forest disturbance in 2001–2017. Data were downloaded from https://earthdata.nasa.gov/data/near-real-time-data/firms. Data from Russian weather radars (Dyaduchenko et al., 2014) were used only for several events occurred in 2012, 2014, and 2016 to determine the time of storm event causing windthrow.

3 Structure of the GIS database

The compiled database of stand-replacing windthrow events in the forest zone of the ER in 1986-2017 is publicly available at https://doi.org/10.6084/m9.figshare.12073278.v6 (Shikhov et al., 2020). We divided the spatial and attributive information on windthrow events into three hierarchical levels that correspond to three GIS layers, i.e., three shapefiles (.shp), in the database:

- "Elementary damaged area" (EDA), that is a single-part polygon of wind-damaged forest;
- "Windthrow area", that represent a group of closely spaced wind-damaged areas, i.e., a multipart polygon, associated with one storm event;
- "Storm event track", that is a cluster of windthrow areas having similar direction and the same date (or same date range) of occurrence, which were most likely induced by one convective or non-convective storm.

GIS layers have WGS84 geographic coordinate system (EPSG:4326). The key fields *ID* and *storm_ID* associates each damaged area with the spatial features in the datasets of windthrow and storm event tracks respectively using one-to-many relation. ID values of windthrow areas are set according to the date of occurrence of storm events. Within one year, numbers are first set for windthrow areas with known dates, and then for ones with unknown dates. If two or more windthrow areas are caused by one storm event, their numbers are sequential according to storm movement direction. The numbering of EDAs is organized according to the numbering of windthrow areas. EDAs related to one windthrow area are numbered from the lower left corner, that is, from southwest to northeast. The structure of the attribute tables of each shapefile (stored in .dbf files) is presented at Tables 1–3. The determination process of the presented characteristics is described in Section 4 and schematically presented at Fig. 2. Figure 3 shows an example with all three hierarchical levels of the database.

4. Methods: windthrow delineation and parameters determination

The process of windthrow identification and attribution to a particular type includes four stages (Fig.2): (1) delineation of a windthrow using the Landsat-based GFS and EEFCC products or time series of the Landsat or Sentinel satellite images, (2) subsequent verification of a windthrow using the HRI and determination of the type of a storm event causing a windthrow, (3) estimation of geometrical characteristics of a windthrow, and (4) determination of storm date or range of dates by utilizing additional information. Most of data collection stages were performed manually using standard GIS tools, except for the data extraction from the GFC and EEFCC products and calculation of the geometrical characteristics of windthrow areas (that were automated with Python language). Due to several limitations of the data sources and the use of expert knowledge at different stages of the data collection workflow (Fig. 2), the compiled database is spatially and temporally inhomogeneous and hence incomplete. In particular, the database lacks small-scale forest disturbances with area below thresholds (Fig. 2). The main data and method limitations are discussed in Section 6.

4.1 Delineation of windthrow areas

4.1.1 GFC-based delineation (2001-2017)

We systematically searched through the GFC dataset for forest loss areas that have characteristic windthrow-like signatures. The search was performed for each cell of a supplemental grid with 50 km cell size that was built for the ER. In particular, we looked for forest disturbances with the shape stretched along the direction of storm or tornado movement. Wind-related

forest disturbance rarely have quasi-circular/elliptic or regular shapes that are characteristic for fire-related disturbance and logged areas, respectively (Shikhov and Chernokulsky, 2018, Shikhov et al., 2019). Windstorm- or snow/icestorm-caused windthrow areas have amorphous spatial structure and a varying degree of forest damage, whereas tornado-induced windthrow areas have quasi-linear spatial structure and almost total removal of a canopy (Chernokulsky and Shikhov, 2018). After selecting an area affected by a windthrow, we extracted respective pixels from the GFC data and converted them from raster to multipart vector polygons, which consist of many singlepart polygons, so-called 'elementary damaged areas' (EDAs, fig. 2, fig. 3). We removed all EDAs with an area ≤ 1800 m^2 that equals to area of two GFC pixels. We filtered out such small-scale disturbance since it is virtually impossible to confirm their wind-related origin. Moreover, the area of local windthrow can be almost three times overestimated by Landsat images (Koroleva and Ershov, 2012). We found, that the absence of minimum accepted area for EDAs will increase area of windthrow by 2-3% on average (up to 6% for several windthrow areas with amorphous spatial structure). However, the number of EDAs mistakenly referred to windthrow can be substantially overestimated.

In total, we delineated 450 windthrow areas using the GFC dataset, and clarified contours of 126 of them manually using the Landsat, Sentinel-2 images, or the HRI (see Section 4.2 for details).

4.1.2 EEFCC-based delineation (1986–2000)

For the EEFCC data, we performed similarly to the GFC searching and delineation of windthrow areas with however some limitations. The main limitation is related to the classification of forest losses into broad periods, i.e., 1986-1988 and 1989-2000. Thereby, windthrow area can be correctly delineated only if it lacks overlap with other forest disturbances, namely loggings and wildfires, occurred in the same period. For instance, in highly-populated areas, salvage loggings are usually performed in 1–2 years for most of wind-damaged forests. Such windthrow areas were delineated by the Landsat images with a semi-automated NDII-based method (see Section 4.1.3). Based on the EEFCC, we were able to delineate windthrow areas with high confidence mainly in the low-populated northern part of the ER (Fig. 4). To partially avoid missing of windthrow areas, using Landsat images, we performed additional verification of all large-scale forest loss areas (with area more than 5 km^2) in highly-populated regions independently of their geometry, since windthrow areas can be totally masked out by logged areas. We were able to find three large-scale windthrow areas (≥ 10 km^2) in these regions. However, some windthrow events can still be missed.

In total, we delineated 153 windthrow areas using the EEFCC dataset. Contours of the 32% of them were then substantially clarified manually with the Landsat images, obtained before and after the storm events. Another 22 windthrow areas that occurred before 2001 were delineated manually using the Landsat images. As for the GFC data, we removed all EDAs with an area < 1800 m^2, since it is often impossible to confirm their wind-related origin.

4.1.3 NDII-based delineation (1987-2000)

We used Landsat TM/ETM+ images (Level 1T) obtained before and after the storm event in the growing season to delineate seven large-scale windthrow, occurred before 2001. We used the difference of Normalized Difference Infrared Index (NDII, Hardisky et al., 1983) to detect and delineate wind-related disturbance. High efficiency of the NDII-based windthrow identification on Landsat images has been shown previously (Wang et al., 2010; Wang and Xu, 2010; Chernokulsky and Shikhov, 2018). The NDII was formulated as follows:

$$NDII = (TM4 - TM5)/(TM4 + TM5), \quad (1)$$

where TM4 and TM5 are the reflectance in the bands 4 (0.85 μm) and 5 (1.65 μm) of the Landsat TM/ETM+ data, while the difference was calculate as $\Delta NDII = NDII_{before} - NDII_{after}$, where subscripts 'before' and 'after' denotes two closest to an event cloud-free images obtained, respectively, before and after the windthrow occurrence, but in the growing season only.

We applied none atmospheric correction algorithm for pre-processing Landsat images, since the NDII is based on the near-infrared (0.76 - 0.90 nm) and middle-infrared (1.55 - 1.75 nm) spectral bands that are almost insensitive to atmospheric impact. For the NDII-based delineation process, we used only images with cloudiness less than 10% based on the CFMask algorithm (Foga et al., 2017). For other purposes (verification, type and date determination), we visually inspected Landsat images for lacking clouds over the area of interest (i.e., a windthrow area).

The masking of forested lands was performed on the 'before' image with the use of Iterative Self-Organizing Data Analysis Technique Algorithm (Ball and Hall, 1965) unsupervised classification. Then, the NDII was calculated only within the mask of the forested area. The same technique was successfully applied previously to delineate windthrow areas caused by the 1984 Ivanovo tornado outbreak (Chernokulsky and Shikhov, 2018).

Windthrow and other forest disturbances are characterized by a sharp decrease of the NDII. However, threshold values of ΔNDII for distinguishing between stand-replacing disturbance and moderate damaged or undamaged forests, differ for each pair of images. We estimated threshold value from the statistics of ΔNDII raster. Firstly, we obtained the mean value and standard deviation of ΔNDII within the entire forest-covered area on image. Stand-replacing forest disturbance inherently has ΔNDII values substantially higher than the image average. To separate stand-replacing forest disturbance from other forest-covered area, we used the threshold value of two standard deviations, which was previously tested by Koroleva and Ershov (2012). However, in some cases the ΔNDII distribution within the entire image was skewed (e.g., due to the presence of cloud decks or haze on the post-event image). In such cases, we lowered the threshold value of ΔNDII iteratively by comparing the detected changes with results of visual identification of windthrow on a post-event image (using several examples located in different parts of windthrow). As a result, actual threshold values ranged from 1.5 to 2 standard deviations. Then, a binary raster of detected changes (i.e., forest losses) has been created (see fig. 5d) and converted to a shapefile. At the next step, windthrow areas were separated from logged areas and other disturbances (see Section 3.2). The EDAs ≤ 1800 m^2 were removed. Figure 5 presents the example of the NDII-based identification of the aftermath on 21 June 1998 Moscow windstorm (Los Angeles Times, 1998).

4.1.4 Combining delineated polygons to a windthrow areas and windthrow areas to a storm event tracks

In general, a group of closely spaced EDAs, caused by one storm event, was assigned to one windthrow. By the 'close distance' we meant in most cases a distance of tens or hundreds of meters between the nearest EDAs. This distance is determined manually by the proportion of stand-replacing damage, and the presence of treeless areas. Maximum distance between nearest EDAs combined to one windthrow area may reach 10 km, if a windthrow crossed treeless areas.

Most of windthrow areas were extracted from the GFC dataset (450), the EEFCC dataset (153), or with the NDII-based methods (7). These windthrow areas were first automatically delineated as a multi-part polygons, and then we specified exact contours of their components — single-part polygons (EDAs). After that, we correctly merged them to a windthrow itself (Fig. 2). We delineated other 90 windthrow areas manually using the Landsat, Sentinel-2 images, or HRI — 30, 17, and 43 windthrow areas, respectively. In this case, we first delineated EDAs and then merged them into a windthrow.

Many storms induced a series of successive windthrow areas, which are separated from each other by tens or even hundreds of kilometres of undamaged forests, treeless areas or water bodies (Fig. 3). In general, we divided the damaged areas into two separate windthrow (two records in the dataset), if the gap between them exceeded 10 km. This threshold is based on the study of Doswell and Burgess (1988), who proposed the 5–10 miles (8–16 km) threshold for the gap to discriminate between one skipping tornado and two successive tornadoes. A few exceptions were associated with changes of windthrow direction, transformations of one windthrow type to another identified by the HRI, i.e., the tornado-induced to non-tornado-induced, and with abrupt change of forest damage degree — from 60–80% to 5–10% of stand-replacing disturbance. In these cases, the distance between two distinct windthrow areas was less — for instance, the minimum distance was about 1 km when a tornado-induced windthrow transformed to a squall-induced one.

If several close windthrow areas have similar direction, differing by no more than 30°, and the same date (or date range) of occurrence, we assigned them to one storm event. We highlight successive and parallel windthrow areas (Fig. 3). Successive windthrow areas induced by one storm event follow downwind one after another and approximately fall on one straight line (the angle of deviation from this line does not exceed 10-20°). Such windthrow are presumably induced by one convective cell generating a sequence of squalls or tornadoes. In contrast, parallel windthrow areas that located within one storm event are situated parallel to each other (with an angle less than 30°). They are presumably associated with two or more different convective cells or mesocyclones, generating squalls or tornadoes, often embedded into one mesoscale convective system.

The expert-based process of windthrow areas combining to a storm event was based as well on various additional information including the storm dates and types (see next sections), information from weather station reports, eye-witness and newspaper reports, data from meteorological satellites, and so on. In total, the dataset of storm event tracks contains 486 items.

4.2 Verification of windthrow events and determination of its type

We verified each windthrow area in the database using pre- and post-event Landsat/Sentinel-2 images, high-resolution images and additional information. This verification was performed to ensure the forest disturbance was caused by wind and to determine a type of a storm caused a windthrow. In total, we verified 54% of windthrow areas with the HRI, mainly for the 2001-2015 period. Other events were verified using the Landsat images (22% of windthrow), the Sentinel-2 images (9%) and additional data sources like weather station and eye-witness reports (15%). As a result, the probability that any forest disturbance was mistakenly referred to windthrow is minimal.

In addition, we used the last cloud-free Landsat or Sentinel-2 image obtained before a storm and first image obtained after it to separate windthrow areas from other disturbance, mainly from logged areas. We removed forest disturbance that were not related to a storm event (Fig. 6). During the verification, we also found and delineated several storm-damaged areas that were missed in the GFC/EEFCC data. Such areas are located mainly in small-leaved or broadleaved forests. After the verification, we determined the type of a windthrow depending on a weather phenomenon induced this windthrow. We selected tornado-induced and non-tornado-induced windthrow areas, the latter were subdivided into induced by convective and by non-convective storms. In turn, non-convective storms include also snowstorms, which are indicated in the database but not analyzed separately further in the paper. By convective storms we mean squalls and downbursts; however, this more detailed division lacks in the database.

To distinguish tornado-induced windthrow areas from other wind-related disturbance, we determined the direction of fallen trees using the HRI. Indeed, the main signature of tornado-induced windthrow is the counterclockwise, or infrequently clockwise, rotation of the fallen trees (Beck and Dotzek, 2010; Shikhov and Chernokulsky, 2018). In the lack of the HRI, we considered three additional signatures of tornado-induced windthrow, namely (1) quasi-linear structure of a windthrow with a ratio of length and width $\geq$ 10:1, (2) a gradual turn of a storm track, and (3) predominately total removal of forest stands (Shikhov and Chernokulsky, 2018; Shikhov et al., 2019). Note, that the ratio of length and width of tornado track $\geq$ 10:1 is also typical for U.S. (Schaefer and Edwards, 1999). Based on these three signatures and additional information from weather station reports, witness reports, photos and videos, we assigned the high or medium degree of certainty of storm type determination for each windthrow (Table 4).

Windthrow areas, caused by non-convective windstorms or snowstorms, have as well specific geometrical features that seen at satellite images. Specifically, windthrow areas related to non-convective windstorms typically have enormous length and width of the damage track, up to 200 and 45 km respectively, with however slightly or moderate degree of forest damage. Stand-replacing disturbance caused by non-convective windstorms are usually occur in dark coniferous forests only (Dobbertin et al., 2002; Schmoeckel and Kottmeier, 2008). Since non-convective storms affect large areas and last for relatively long period, they are typically well-reported by weather stations, which simplify the attribution of related windthrow. In its turn, snowstorm-induced windthrow areas are distinguishable from other disturbance primarily based on the dates of occurrence — they happen usually in autumn; although, one severe snowstorm occurred in early summer. It is of note, that we found none of snowstorm-induced stand-replacing windthrow happen in winter.

After the determining of a storm event type, we excluded from the database the tornado-induced windthrow with an area ≤ 0.05 km^2 and other windthrow with an area ≤ 0.25 km^2. We took into account the following reasons during exclusion of such small-scale windthrow areas:

1. Difficulty to prove that these disturbances were actually caused by wind, especially in the lack of the HRI.
2. Difficulty to determine storm event dates with the Landsat images for these windthrow areas.
3. High uncertainty of estimated geometrical characteristics of small-scale windthrow (Koroleva and Ershov, 2012; Shikhov and Chernokulsky, 2018).

Only five squall-induced windthrow with an area < 0.25 km^2 were stored in the database, since they are associated with severe weather outbreaks with proven dates. It is of note, that a typical tornado-induced windthrow consist of a relatively small number of EDAs with total removal of forest stands that are well-detected by the Landsat images. In its turn, a typical non-tornado-induced windthrow include larger number of small-scale (i.e., 2-4 Landsat pixels) areas of stand-replacing disturbances, that are worse detected by satellite images. This difference results in the necessity of using two distinct thresholds for tornado- and non-tornado-induced windthrow areas.

The threshold values used in Sections 4.1–4.2 have some subjectivity, and their modification may substantially change the number of allocated windthrow areas in the dataset. The optimization of above-described threshold values can be evaluated in further studies that should involves ground-based data.

4.3 Estimation of geometrical parameters of windthrow areas and storm tracks and its accuracy

We used the Landsat data and the Landsat-based products GFC and EEFCC to estimate geometrical parameters of windthrow areas. We determined the path length (L), mean and maximum widths (W_{mean} and W_{max}), and damaged area (A) for each windthrow using the technique that had been successfully implemented for tornado-induced windthrow areas (Shikhov and Chernokulsky, 2018). The calculation of these parameters was performed in the Lambert Equal Area and Equidistant projection for North Asia to avoid possible projection-related distortions.

We calculated A in the ArcGIS 10.4 as the sum of area of forest damaged plots, which are attributed to one windthrow. We determined L as a length of the central line drawn through a damaged area, i.e. distance between two farthest points of a windthrow. The central line was created automatically (using a Python tool) as a distance between two farthest points of a windthrow. It is insensitive to the allocation of patches to windthrow area.

We calculated W_{mean} as the mean length of several transects that are perpendicular to a storm track with a 200 m step; this step had been found optimal in terms of quality and counting efficiency (Shikhov and Chernokulsky, 2018). Only stand-replacing windthrow areas were taken into account in this calculation. In comparison to (Shikhov and Chernokulsky, 2018), where W_{max} were calculated manually using the HRI data, in this study, we assigned the length of the largest transect to W_{max} because the lack of the HRI for many windthrow areas.

In addition to windthrow characteristics, we estimated geometric characteristics of EDAs and those of storm tracks. Particularly, for EDAs, we calculated their area A_{EDA}. For storm tracks, we estimated maximum and mean width (W_{TRmean} and W_{TRmax}), path length (L_{TR}), and damaged area (A_{TR}). We calculated W_{TRmean} based on the same transects that were used to calculate W_{mean} but without excluding undamaged forests and treeless areas. Similarly, length of the largest transect that includes undamaged forests and treeless areas was assigned to W_{TRmax} (Fig. 7). If a track consists of two (or more) parallel windthrow areas, then its width was calculated within the outermost boundaries of these windthrow areas (Fig. 3). The same calculation was performed for L_{TR} in case of two (or more) subsequent windthrow areas (Fig. 3). Thus, the used 10-km threshold (see Section 4.1.4) may influence geometrical characteristics of single windthrow area, but do not affect those of a storm event.

We assessed the accuracy of GFC-based estimates of windthrow geometrical parameters by comparing them with the same parameters calculated manually with the use of HRI. We performed such procedure for ten windthrow areas caused by squalls, whose area ranges from 0.26 to 6.09 km^2 (Table 5). Distribution of their A is close to the one for the full dataset.

We delineated manually all EDAs within these ten windthrow areas using the HRI. In total, we found 837 and 947 EDAs, according to the GFC and the HRI data respectively. Owing to relatively correct georeference of the Landsat data (Landsat Collection 1, 2019), we found no systematic spatial bias between contours of GFC-based and HRI-based windthrow areas. Despite their general matching, there is no complete overlap due to different spatial resolution of the GFS and HRI (Fig. 8). For example, one GFC-based EDA may intersect with several HRI-based ones, and vice versa. We found, that only 66.5% of the total area is attributed to windthrow in both GFC and HRI, while EDAs with small area can be missed. In particular, 263 HRI-based EDAs with the total area of 0.97 km^2 were completely missed in the GFC, while 146 GFC-based EDAs with the total area of 0.52 km^2 were missed in the HRI. For overlapped EDAs, we found the mean absolute error and root mean square error of A_{EDA} estimates amounted to 27.6% and 13.1%, respectively. We found that the relative error decreases for large EDAs and for those having a simple shape, i.e., quasi-circular. The user's and producer's accuracies increase from 20–25% for EDAs with A_{EDA} < 0.01 km^2 to 70–75% for EDAs with A_{EDA} > 0.1 km^2. In general, for the overlapped EDAs, the GFC overestimates their A_{EDA} (by 4% on average) primarily in coniferous forests. Mutual effect of more frequent omission of small EDAs in the GFC compare to the HRI and overestimation of overlapped EDAs results in approximate equality of total area of delineated windthrow — 17.11 km^2 and 17.13 km^2 based on the GFC and HRI, respectively.

For entire windthrow area, we calculated as well an accuracy of their geometrical characteristics estimates. In particular, we calculated the user's and producer's accuracies of the GFC-based delineation for each of ten selected windthrow. These accuracies are mainly determined by the complexity of windthrow shapes and composition. In particular, the accuracy is higher for a windthrow consisting of relatively small number of simple-shape EDAs. Otherwise, the accuracy decreases down to 50% for a windthrow having very amorphous spatial structure. In our sample, the GFC data tends to overestimate the area of windthrow — eight cases out of ten were overestimated. The mean absolute percent error (MAPE) for A is 14.6%. The major overestimation of A by the GFC data, as well as W_{mean} and W_{max}, was revealed for relatively small windthrow areas. This is in line with the previous findings by Koroleva and Ershov (2012). They showed that the reliable

estimate (with 15% accuracy) of the damaged area using the Landsat images is possible only for windthrow areas exceeding 0.026 km^2. It is of note, that for tornado-induced windthrow areas, Shikhov and Chernokulsky (2018) found, that the GFC data generally tends to underestimate *A*, with MAPE amounted to 17.9%.

The assessment of geometrical parameters of windthrow areas appeared before 2000 and found by the EEFCC is challenging due to the low availability of the HRI or other independent data sources, e.g. the data of forestry services. Windthrow areas induced by storm events that occurred >20 years ago can be delineated by the HRI only if a storm passed through old-growth forests that have not been affected by other disturbances, i.e., timber harvesting or wildfires, in subsequent years. Such forests are widespread only in the northeastern part of the ER (Pakhuchiy, 1997). We found five EEFCC-based windthrow occurred between 1998 and 2000 that were most well-detected by the HRI — four tornado-induced and one storm–induced windthrow. We delineated them with the EEFCC and HRI and compare their characteristics (Table 6). We found general overestimation of *A*, W_{mean} and W_{max} in the EEFCC, that was larger than in the GFC. It may be related to the inclusion into a windthrow not only real wind-damaged area but also surrounding pixels where trees had died after a storm event mostly because of bark beetles (Köster et al., 2009). Intensity of this mortality is highest at a second year after a storm event (Köster et al., 2009).

4.4 Determination of windthrow dates

We aimed to establish the exact date or even the exact time for each windthrow appearance. However, due to data constraints, dates of some windthrow events were determined with 6 months accuracy. We iteratively refined date, or a date range, by using different data. The process, related to the determination of date of tornado-induced windthrow only, had been described previously in (Shikhov and Chernokulsky, 2018).

First, the year of a windthrow can be obtained directly from the Landsat products but with some limitations. In the GFC, forest disturbance are accompanied with information on the year of event occurrence. However, the exact year is determined correctly only for 75.2% of forest loss pixels; for 24.8% of them, the date can be either 1–2 year earlier or later (Hansen et al., 2013). In the EEFCC, a year of windthrow occurrence is not explicitly determined and came within the ranges 1986–1988 and 1989–2000 years.

Next, we refined a range of dates based on all available images from the Landsat and Sentinel-2 satellites. The accuracy of such refinements depends on a frequency of observations and cloudiness. The availability of cloudless Landsat images varied from year to year. The lowest number of cloud-free images (2–4 images a year on average) is available for 2003–2006 and 2012, when only Landsat-7 (SLC-off) data are available (Potapov et al., 2015). Hence, the worst accuracy of windthrow date determination is typical for these years. On average, 8-10 images per year can be used for windthrow dates determination. Due to Sentinel-2A satellite launching, number of images per year had an abrupt increase after the summer of 2016. We used images taken throughout a year. Despite the frequency of cloudless images in autumn and winter was lower than in summer season, it was sufficient for analysis. Thus, wintertime images (of land covered with snow) were

successfully used for windthrow identification, especially if a storm occurred at the end of summer season, and autumn season lacked cloud-free images.

Further, given the satellite-derived range of event possible dates, we made the subsequent analysis using additional data such as weather station observations, various databases and reviews on hazardous weather events, damage reports, photos and videos in the media and social networks, and reanalysis data (see (Shikhov and Chernokulsky, 2018) for details). This analysis allowed to establish the exact dates for 48.4% of all windthrow events including 39.2% and 59.7% of tornado- and non-tornado-induced windthrow events, respectively.

The dates of storm-induced windthrow events were defined more successful than those for tornado-induced ones due to the local nature of convective storms, especially of tornadoes, and a relatively large distance between Russian weather stations. Specifically, the average and median distance between nearest weather stations within the study area amounted to 53.7 and 49.9 km, respectively. Wherein, many storm events were reported by weather stations located on a storm path at a distance of 50-100 km from a windthrow, while the closest stations did not reported strong wind gusts since they were away from a storm path. In total, we matched storm reports of weather stations, namely reports with wind gusts ranges from 15 m/s to 34 m/s, only with 34.5% of windthrow events with known date.

Another reason for more successful determination of dates of appearance for large-scale windthrow areas than for small-scale ones, e.g., tornado-induced, is an increase of probability that a corresponding storm passes through a settlement(s) and this is covered in the media. In total, we used media reports, information from regional weather services, witness photos and videos, existed scientific literature (e.g., Dmitrieva and Peskov, 2013; Petukhov and Nemchinova, 2014; Shikhov and Chernokulsky, 2018; Shikhov et al., 2019) to specify the date and time of 29.7% of windthrow events.

Dates and time of some cases (7.8% of all cases) were established using images from meteorological satellites Terra/Aqua MODIS and METEOSAT-8, and Russian weather radar data (Dyaduchenko et al. 2014). However, the routine usage of these data is time-consuming and limited due to some access restrictions. Subsequent clarification of windthrow exact time can be carried out in further studies.

5 Results and discussion

5.1 Windthrow type

The compiled database includes three shapefiles (.shp), corresponding to three hierarchical levels such as elementary damaged areas, windthrow, and storm events. The database includes 102747, 700, and 486 objects for each level, respectively. The total area of the spatial features is equal 2966.1 km^2. It is of note, that we cannot determine whether the trees were felled or broken by the wind based on satellite images, even having very high resolution. Therefore, we use a single term “windthrow” for all types of wind-induced forest damage.

The overwhelming majority of found stand-replacing windthrow in ER, namely 97.4% of the events and 95.3% of wind-damaged area, are associated with convective storms and tornadoes (Table 7). More than a half of all windthrow events are

tornado-induced with however relatively small damaged area (less than 13% of the total wind-damaged area). Non-convective storms and snowstorms are responsible for less than 5% of the area of stand-replacing windthrow in ER. This is somewhat in contrast to Western and Central Europe, where most of forest damage is induced by non-convective wind events, namely winter storms, caused by strong extratropical cyclones (Gardiner et al., 2010; Gregow et al., 2017). Indeed, winter windstorms affects less Eastern Europe compare to Western and Central Europe (Haylock, 2011).

Among 486 storm events that caused windthrow, 381 yielded only one windthrow area (Fig. 9), primarily tornado-induced. The rest 105 storms resulted in a smaller number of windthrow events (319) but larger damaged area — 2276.6 km^2, namely 76.8% of all damaged area. Most of these storms induced two or three successive or parallel located windthrow areas, and only 14 of them caused ≥ 5 ones. We found maximum of 17 separate windthrow areas that related to one storm. We found 71 storm events result in two or more successive windthrow areas, while 12 storm events lead to formation of two or more parallel windthrow areas, and 22 storm events include a family of both parallel and successive ones (fig. 3). The maximum distance between two nearest successive and two parallel windthrow areas amounts to 150 and 26 km, respectively.

It should be noted, that a single storm may cause both tornado- and non-tornado induced windthrow, e.g. a supercell can lead to formation of a tornado and a rear-flank downdraft (Karstens et al., 2013) both causing forest damage. In total, we found 30 storms that resulted in formation of two types of windthrow.

We managed to match several storm events with storm reports at weather stations, in particular the database contains 89 such cases. Among these 89 station reports, we found eight reports with wind gusts ≥ 30 m/s, 14 reports with wind gusts 25-29 m/s, and 30 reports with wind gusts 20-24 m/s. This information has been included in the database, and can be used in further studies to estimate the critical wind speed causing windthrow and to analyse the role of other accompanying weather phenomena, e.g. with snow, heavy rainfall, large hail, etc.

5.2 Spatial distribution of windthrow areas

Windthrow events occur in the entire forest zone of the ER (Fig. 10). However, the highest density is observed near the 60° N and somewhat coincides with the highest percentage of forest-covered area (see Fig. 1). It is of note, that two windthrow areas are located north of 66° N and one of them is even north of the Arctic Circle. The dominant direction of both tornado-induced and other windthrow is SW-NE (Fig.15b), which is in line with the previous studies on tornado climatology in Northern Eurasia (Shikhov and Chernokulsky, 2018; Chernokulsky et al., 2020).

Three regions, where windthrow has affected more than 0.75% of forests, can be highlighted (Fig. 11a). Two of them are related to the catastrophic storms which occurred on 27 June 2010 and 29 July 2010. In total, these two storms have damaged 1140 km^2 of forests, which is 38.4% of the total area of stand-replacing windthrow in the ER in 1986–2017. The third area is located on the western slope of the Northern Ural and coincides with the largest massive of dark-coniferous forests in the ER (Pakhuchiy, 1997). The most important windthrow events occurred here in June 1993, July 2012 and October 2016. The latter was induced by snowstorm. The relatively high frequency of windthrow in this region was emphasized previously (Lassig and Mocalov, 2000; Shikhov and Chernokulsky, 2018; Shikhov et al., 2019). It was

hypothesized that it may be related to the combination of several factors, namely widespread old-growth forests, a high annual precipitation rate (up to 1000 mm per year), and large soil wetness, which all contribute to the forests wind susceptibility (Dobbertin, 2002).

The highest density of tornado-induced windthrow is found between 59° and 62° N, 48° and 56° E (Fig. 11b), which is in a good agreement with the previous estimates (Shikhov and Chernokulsky, 2018). However, the ratio of tornado-damaged area to the total forested area is higher in the western part of the ER (Fig. 11b). It is of note, that higher values of so-called convective instability indices are also observed in this region (Taszarek et al., 2018).

The species composition and age of forest stands have substantial influence on the spatial distribution of windthrow (Dobbertin, 2002, Suvanto et al., 2016; Gregow et al., 2017). Using the presented dataset, estimates of relationship between windthrow area and forest stands characteristics can be carried out in future studies at a regional scale.

5.3 Temporal variability of windthrow and storm events

We successfully determined the year of occurrence for all windthrow events and the month of occurrence for 263 (67.9%) tornado-induced and 224 (71.5%) non-tornado-induced windthrow events. We established the dates of occurrence for 339 windthrow events, including 149 tornado-induced (39.2%) and 187 (59.7%) non-tornado-induced ones. It is of note, that the dates of most impactful large-scale windthrow with damaged area > 10 km^2 were determined for 44 out of 49 cases (90%). Windthrow events with known dates have a total area of 2599 km^2, i.e., 87.7% of the total wind-damaged area.

The storm-damaged area has a relatively high inter-annual variability (Fig. 12). The largest area of windthrow, i.e. >1200 km^2, is found in 2010, when two exceptional storm events occurred. An extremely high number of tornado-induced windthrow events occurred in 2009 and 2017. Storm events causing windthrow have been observed every year and ranges from 2 to 36, with the maximum in 2012 and minimum in 2001. In general, annual number of windthrow and storm events was lower before 2001 when the EEFCC data were used to identify windthrow, and higher after 2001, when the GFC data were utilized. Annual number of windthrow events for these periods amount to 12.1 and 30.5, respectively; in its turn, annual number of storm events amounts to 8.3 and 20.9. This temporal inhomogeneity, related to different initial data used, should be taken into account when inter-annual variability is analyzed. More details on the dataset limitations are provided in Section 6.

Windthrow events occur in the ER from May to October (Fig. 13). The seasonal maximum of the number of windthrow events is found in June — both for tornadoes and for other storm events. This is in concordance with the previous estimates on the tornado climatology (Shikhov and Chernokulsky, 2018; Chernokulsky et al., 2020). Maximum frequency of the occurrence of storm events causing windthrow is also observed in June. Moreover, more than 90% of storm events with known dates occur in summer. It is important to note, that we failed to establish the month of appearance for 127 tornado-induced windthrow areas and 98 non-tornado induced ones, which have total area of 245 km^2.

Sometimes, two or more storm events causing windthrow occurred in the ER on the same day. In total, we found seven outbreaks with more than ten windthrow areas per day. The most remarkable outbreaks occurred on 18 July 2012 when nine

storms resulted in 25 windthrow areas, and on 7 June 2009 when five storms resulted in 24 windthrow areas. However, the largest forest damage is associated with a single storm, namely the long-lived convective storm "Asta" (Suvanto et al., 2016). This storm has passed over the northwestern part of the ER and Finland on 29 July 2010 and has damaged 639 km^2 of forests in Russia only.

No winter windthrow events were found. It is of note, that both GFC and EEFCC Landsat-based products reveals stand-replacing windthrow area regardless of the season of its appearance. In particular, if windthrow happened in winter it would be clearly seen on image taken in subsequent vegetation period because of rather slow forest recovery process. Therefore, the revealed lack of winter windthrow is feasible due to the climatic conditions of the study area and does not associated with data limitations. In particular, winter storms from Western Europe reach the territory of Russia already weakened (Haylock, 2011), In addition, in the ER and Northern Europe, while low temperatures and soil freezing also prevents trees from falling because of windstorms during winter season (Suvanto et al., 2016). According to (Suvanto et al., 2016), winter windthrow are not typical for Finland as well.

We restored the time of occurrence with 6-h accuracy for 216 windthrow events — 136 among them using weather station reports and 80 using other data sources. We found 122 windthrow events (56.4%) occurred between 15.00 and 21.00 of local time, which coincides with the afternoon maximum of the development of a deep convection. However, several most impactful storms, including for instance the 'Asta' storm, occurred around midnight at local time. No windthrow found between 06.00 and 10.00 local time during the morning minimum of the convection diurnal cycle. The similar diurnal cycle was found for tornado events in the Northern Eurasia (Chernokulsky et al., 2020).

5.4 Geometrical parameters of windthrow areas, elementary damaged areas, and storm tracks

Area of EDAs varies between 0.0018 to 30.9 km^2. Most of EDAs are less than 0.01 km^2 (Fig. 14a), but their total area is less than 10%. In turn, 1% of the largest EDAs account for 36.8% of the total area of windthrow. Using the Kolmogorov-Smirnov (K-S) test, we found that at 0.01 significant level we can reject the null hypothesis that two samples of A_{EDA} within each pair of windthrow types are drawn from the same distribution (at 0.01 level). Because of small sample size of windthrow areas induced by non-convective storms, later in the article we will not discuss the results of the K-S test to compare distributions of characteristics of this type with those of other types.

Tornado-induced windthrow areas contain fewer EDAs, than windthrow areas induced by strong wind (Fig. 14b). Particularly, most of tornado-induced windthrow areas include 10–25 EDAs, and only 2.5% of them consist of more than 100 EDAs. In contrast, about 43% of non-tornado induced windthrow areas includes more than 100 EDAs, while 5.5% of them consist of more than 1000 EDAs. Based on the K-S test, we found that samples of number of EDAs in tornado- and convective storm induced windthrow areas are from different distributions.

A relatively small number of severe storm events are responsible for most of the area of windthrow (Fig. 15a). Indeed, the ten most destructive storm events occurred in the ER over 1986-2017 damaged 1758 km^2 of forests, namely 59.2% of the

total area of windthrow in the database. This peculiarity is less pronounced for tornado-induced windthrow areas, since their area usually is less than 10 km^2. Particularly, ten tornadoes with the largest area damaged 96.6 km^2 of forests — 25.5% of the total tornado-damaged area. Thus, the distribution of tornado-damaged area is less skewed to high values, than the distribution of other windthrow areas. The K-S test shows that samples of *A* for tornado- and convective storm induced windthrow areas are from different distributions.

Length of windthrow ranges from 0.8 km to 283.6 km (Fig. 15b). More than 44% of tornado-induced windthrow areas have path length < 5 km, while path length 5-15 km is most frequent for non-tornado-induced ones. Based on the K-S test, we found that samples of number of *L* for tornado- and convective storm induced windthrow areas are from different distributions. The maximum length of storm track, consisting of several subsequent windthrow areas, reaches 544 km. This damage track is caused by the storm on 27 June 2010. In addition, another nine storm tracks have a length exceeding 250 km — most of them are among the most destructive in terms of forest-damaged area. Such series of windthrow with an exceptionally long path length were likely caused by derechos. Derechos are long-lived mesoscale convective systems producing widespread damaging winds and causing large-scale forest damage in U.S. (Johns and Hirt, 1987; Peterson, 2000), Europe (Taszarek et al., 2019), and South America (Negrón-Juárez et al., 2010). Although, not a single derecho event have been reported previously in Russia. A more detailed further analysis of these storm events should be carried out to confirm their nature.

Most of tornado-induced windthrow areas have W_{max} and W_{mean} less than 200 m (Fig. 15 c,d). Instead, the distribution of W_{max} of non-tornado induced windthrow areas shifted toward larger W_{max}. In particular, 103 windthrow areas (32.9%) have W_{max} > 1000 m. The K-S test shows that samples of both W_{max} and W_{mean} for tornado- and convective storm induced windthrow areas are from different distributions. Width of storm tracks is several times higher than the width of windthrow areas. Moreover, the W_{TRmax} of windthrow areas caused by non-tornadic storms is several times higher than the W_{TRmean}. W_{TRmax} exceeds 30 km for three widest convective storms — two derechos occurred on 27 June 2010 and 29 July 2010, and one non-convective storm occurred on 7-8 August 1987.

6 Data and method limitations

Due to several data and method limitations, the presented database is spatially and temporally inhomogeneous and hence incomplete. Specifically, since most of windthrow were delineated from the GFC and EEFCC datasets, forest loss areas which are initially missed or underestimated in these datasets, could be as well missed in our database. The verification performed with the Landsat images and the HRI allows to reduce these omissions. In particular, we found several windthrow in small-leaved or broadleaved forests that were substantially underestimated in the GFC dataset.

The efficiency of the method depends on the percentage of forest-covered area. In general, our data is more complete for low-populated northern and eastern part of the ER, where forests cover 70–90% of the territory and dark-coniferous forests

are widespread (Bartalev et al., 2016). However, some regions in the northern part of the ER are not covered by HRI which prevents from thorough verification of some windthrow areas.

In the southern part of the study area, the dataset is likely less complete since some windthrow areas can be overlooked. In particular, it is possible to miss windthrow area if a storm or tornado passed through areas of intensive timber harvesting or agricultural lands (Shikhov and Chernokulsky, 2018). Salvage logging performed shortly after a storm event also complicates the identification of wind-related forest damage (Baumann et al., 2014). However, in most cases, the time interval between storm event and salvage logging in the ER was quite long, i.e., more than a year, except for more populated southern regions.

Temporal inhomogeneity of our database, especially for small-scale windthrow areas, comes from the following causes:

1. The use of two different Landsat-based products to search windthrow-like disturbance — the EEFCC before 2001 and the GFC after. The GFC data has higher accuracy of forest loss detection and of initial time assigning, than the EEFCC (see Section 4.1 for details), which allows to detect more windthrow areas. Thus, the annual number of windthrow events 2.5 times higher in the GFC period compare to the EEFCC period.
2. After 2002–2003, the HRI had become available, which made it possible to confirm the tornadic nature of windthrow. The observed increase in the number of tornado-induced windthrow events after 2003 is very likely related to the appearance of the HRI.
3. The start of the Sentinel-2 mission in 2015 providing the images with a 10 m spatial resolution (Drusch et al., 2012) had also increased the possibility for windthrow identification.
4. A strong decrease in the volume of timber harvesting occurred in ER, especially in its northeastern past, after the Soviet Union dissolution (Potapov et al., 2015). This could lead to more omission of windthrow areas in the late 1980s compare to the subsequent period because of their overlapping with logged areas.
5. The number of windthrow areas and storm events has been determined with the use of arbitrary threshold values. It could have changed substantially due to modification of these thresholds (see Sections 4.1.4. and 4.3. for more details). So, the data on the number of windthrow events may be more inhomogeneous than assessment of wind-affected area.

Thus, the presented database should be used for assessing interannual variability with caution. Special assumptions should be made to estimate linear trends. For instance, they can be obtained for particular regions, e.g. for those with little changes of forestry practices, and for relatively large windthrow areas, that are well-detected from both the EEFCC and the GFC data. For instance, linear trend in the number of windthrow with area ≥ 1 km^2 amounts to 0.27 year^{-1} and is statistically significant at 0.05 level[1]. This increase of wind-related forest disturbances is in line with observed increase of such characteristics as convective precipitation (Ye et al., 2017; Chernokulsky et al., 2019), convective cloudiness (Sun et al., 2001; Chernokulsky

[1] Trends were computed with the Theil–Sen estimator. Significance was obtained with the nonparametric Mann–Kendall test.

et al., 2011), convective instability indices (Riemann-Campe et al., 2009; Chernokulsky et al., 2017) in the ER in the last decades.

Currently, the proposed method requires expert verification at almost all stages, which prevents to switch it into the automatic mode. The possibility of automated searching throughout the GFC and EEFCC datasets is limited by a wide variety of windthrow shapes and their overlapping with other forest disturbances. The data collection process requires the use of numerous and diverse sources such as the HRI from various public web-services, weather station reports, eye-witness and media reports, etc.

While the algorithms for automated forest disturbance detection based on satellite data are well-developed and applied at the regional-to-global scale (Huo et al., 2019), automated attribution of forest disturbance to their causes, namely windstorms, logging, wildfires, insect outbreaks, and others, remain a critical challenge for satellite-based forest monitoring. The spectral characteristics of various types of disturbance, e.g., windthrow and logged areas, are often similar (Baumann et al., 2014) that complicates the automated attribution. The promising approaches in this process is the complex use of spectral, temporal, and topography-related metrics (Oeser et al., 2017) as well as implementing of advanced image classification/segmentation methods (Oeser et al., 2017; Liu et al., 2018; Huo et al., 2019). In future studies, such approaches can be applied to automate delineation of windthrow areas in the ER using satellite data with various spatial resolution.

7 Conclusions

The compiled GIS database contains the most complete information on a relatively large stand-replacing windthrow areas in the forest zone of the ER in 1986–2017. The database contains 102747 elementary damaged areas, combined into 700 windthrow areas, which were caused by 486 storm events. For each windthrow, we determined its type with degree of certainty, dates or date ranges, and geometrical characteristics. The database also contains weather station reports and links to additional information on storm events from the media. We included into the database only the stand-replacing windthrow with an area > 0.05 km^2 and > 0.25 km^2 for the tornado- and non-tornado-induced windthrow, respectively.

The total windthrow area amounts to 2966 km^2, namely 0.19% of the forested area within the study region. Most of windthrow in the ER, i.e., 82.5% of the total wind-damaged area, are related to convective squalls and downbursts, which occur mainly in June and July. The ten most impactful storms are responsible for 59.2% of the total forest damage. More than 55% of windthrow events in the database are tornado-induced, but their contribution to total damaged area is much lower — it is less than 13%. Non-convective windstorms and snowstorms caused only 4.6% of storm-damaged area.

The largest area of windthrow is assigned to the 2010 year, when two exceptionally destructive storm events occurred — on 27 June 2010 and 29 July 2010. An extremely high number of tornado-induced windthrow was observed in 2009 and 2017 — 45 and 40 tornadoes, respectively.

The presented method has several limitations resulting in spatial and temporal inhomogeneity of the compiled database specifically for small-scale windthrow areas and hence determine the dataset incompleteness. Because of influence of forest

area percentage and forestry practice, such windthrow areas can be rather missed in the southern part of the ER compare to the northern part. Because of coarser resolution of the EEFCC data and lack of the HRI, windthrow areas can be rather missed before 2001. The obtained increases in number of windthrow events and affected area are mainly artificial.

Despite the incompleteness, the compiled database provides a valuable source of spatial and temporal information on windthrow events in the ER. On the one hand, the database allows estimate the role of wind-related disturbance in comparison with other natural disturbance in forests and improve our understanding of different forest species susceptibility to windstorms. On the other hand, the database presents a unique source of information on storm and tornado events causing forest damage in the ER. It includes numerous of previously unknown storms and tornadoes, which caused forest damage, and also clarifies information on the known storm events. Thus, the database substantially contributes to the climatology of severe storms and tornadoes in the ER. Based on the compiled database, further studies may be carried out to determine the contribution of climate variability to the inter-annual variability of wind-related forest damage, and to quantify the risk of windthrow in forests of the entire ER.

8 Data availability

The data are freely available at https://doi.org/10.6084/m9.figshare.12073278.v6. (Shikhov et al., 2020). It will be periodically updated with new and historical windthrow events.

Author contributions. ASh and ACh designed the study. ASh and ASe performed windthrow identification using satellite data. ASh and IA carried out an analysis of additional information to determine storm event types and dates. Ash and ACh, with contributions by IA, wrote the initial draft of the paper and produced the maps and figures.

Competing interests. The authors declare that they have no conflict of interest.

Acknowledgements. The study was funded by the Russian Foundation for Basic Research (projects no. 19-05-00046 and 20-35-70044). The determination of storm track characteristics was supported by the Russian Science Foundation (project no. 18-77-10076).

References

Attiwill, P. M.: The disturbance of forest ecosystems: the ecological basis for conservative management, Forest Ecology and Management, 63(2-3), 247–300, doi:10.1016/0378-1127(94)90114-7, 1994.

Ball, G. H., and Hall, D. J.: ISODATA, a Novel Method of Data Analysis and Pattern Classification, Stanford Research Institute, Menlo Park, 1965.

Bartalev, S. A., Egorov, V. A., Zharko, V. O., Lupyan, E. A., Plotnikov, D. E., Khvostikov, S. A. and Shabanov, N. V.: Satellite-based mapping of the vegetation cover of Russia, Moscow, Institute of Space Research of RAS, 208 p. 2016. (in Russian)

Baumann, M., Ozdogan, M., Wolter, P. T., Krylov, A. M., Vladimirova, N. A. and Radeloff, V. C.: Landsat remote sensing of forest windfall disturbance, Remote Sensing of Environment, 143, 171–179, doi:10.1016/j.rse.2013.12.020, 2014.

Beck, V. and Dotzek, N.: Reconstruction of near-surface tornado wind fields from forest damage, Journal of Applied Meteorology and Climatology, 49, 1517–1537, doi:10.1175/2010JAMC2254.1, 2010.

Bulygina, O. N., Veselov, V. M., Razuvaev, V. N. and Aleksandrova, T. M.: Description of the dataset of observational data on major meteorological parameters from Russian weather stations (http://meteo.ru/data/163-basicparameters), 2014.

Chernokulsky, A., Kurgansky, M., Mokhov, I., Shikhov, A., Azhigov, I., Selezneva, E., Zakharchenko, D., Antonescu, B. and Kühne, T.: Tornadoes in Northern Eurasia: from the Middle Age to the Information Era, Monthly Weather Review, 148, 3081–3111, doi: 10.1175/MWR-D-19-0251.1, 2020.

Chernokulsky, A., Kozlov, F., Zolina, O., Bulygina, O., Mokhov, I. I. and Semenov, V. A.: Observed changes in convective and stratiform precipitation in Northern Eurasia over the last five decades, Environmental Research Letters, 14, 045001–17, doi:10.1088/1748-9326/aafb82, 2019.

Chernokulsky, A V., Kurgansky, M. V. and Mokhov I. I.: Analysis of changes in tornadogenesis conditions over Northern Eurasia based on a simple index of atmospheric convective instability, Doklady Earth Sciences, 477, 1504–1509, doi:10.1134/S1028334X17120236, 2017.

Chernokulsky, A. V., Bulygina, O. N. and Mokhov, I. I.: Recent variations of cloudiness over Russia from surface daytime observations, Environmental Research Letters, 6, 035202, doi:10.1088/1748-9326/6/3/035202, 2011.

Chernokulsky, A. V., and Shikhov, A. N.: 1984 Ivanovo tornado outbreak: Determination of actual tornado tracks with satellite data, Atmospheric Research, 207, 111–121, doi:10.1016/j.atmosres.2018.02.011, 2018.

Diffenbaugh, N. S., Scherer, M., Trapp, R. J.: Robust increases in severe thunderstorm environments in response to greenhouse forcing. PNAS, 110(41), 16361–16366, doi:10.1073/pnas.1307758110, 2013.

Dmitrieva, T. G. and Peskov B. E.: Numerical forecast with the mesosynoptic specification of extremely severe squalls in the European part of Russia (Case study for June 13 and July 29, 2010), Russian Meteorology and Hydrology, 38(2), 71–79, doi:3103/S1068373913020027, 2013.

Dobbertin, M.: Influence of stand structure and site factors on wind damage comparing the storms Vivian and Lothar, Forest Snow and Landscape Research, 77(1-2), 187–205, 2002.

Doswell, C.A. and Burgess, D.W.: On some issues of United States tornado climatology. Monthly Weather Review, 116, 495–501, 1988.

Drusch, M., Del Bello, U., Carlier, S., Colin, O., Fernandez, V., Gascon, F., Hoersch, B., Isola, C., Laberinti, P., Martimort, P., Meygret, A., Spoto, F., Sy, O., Marchese, F. and Bargellini, P.: Sentinel-2: ESA's Optical High-Resolution Mission for GMES Operational Services, Remote Sensing of Environment, 120, 25–36, doi:10.1016/j.rse.2011.11.026, 2012.

Dyaduchenko, V., Pavlyukov, Y. B. and Vylegzhanin, I.: Doppler weather radars in Russia. Science in Russia, 1, 23–27, 2014. (in Russian)

Foga, S., Scaramuzza, P.L., Guo, S., Zhu, Z., Dilley, R.D., Beckmann, T., Schmidt, G.L., Dwyer, J.L., Hughes, M.J., and Laue, B. Cloud detection algorithm comparison and validation for operational Landsat data products. Remote Sensing of Environment, 194, 379-390. http://doi.org/10.1016/j.rse.2017.03.026, 2017.

Forzieri, G., Pecchi, M., Girardello, M., Mauri, A., Klaus, M., Nikolov, C., Rüetschi, M., Gardiner, B., Tomastik, J., Small, D., Nistor, C., Jonikavicius, D., Spinoni, J., Feyen, L., Giannetti, F., Comino, R., Wolynski, A., Pirotti, F., Maistrelli, F., Savulescu, I., Wurpillot-Lucas, S., Karlsson, S., Zieba-Kulawik, K., Strejczek-Jazwinska, P., Mokroš, M., Franz, S., Krejci, L., Haidu, I., Nilsson, M., Wezyk, P., Catani, F., Chen, Y.-Y., Luyssaert, S., Chirici, G., Cescatti, A. and Beck, P.S.A.: A spatially explicit database of wind disturbances in European forests over the period 2000-2018, Earth System Science Data, 12(1), 257–276, doi: 10.5194/essd-12-257-2020, 2020.

Fraser, R. H.: An analysis of large-scale forest cover disturbance in Canada (1998-2004) based on multi-temporal coarse resolution data, Proc. of the Third Int. Workshop on the Analysis of Multi-Temporal Remote Sensing Images 2005, Art. No. 1469880, 236–240, doi:10.1109/AMTRSI.2005.1469880, 2005.

Gardiner, B., Blennow, K., Carnus, J.-M., Fleischer, P., Ingemarson, F., Landmann, G., Lindner, M., Marzano, M., Nicoll, B., Orazio, C., Peyron, J.-L., Reviron, M.-P., Schelhaas, M.-J., Schuck, A., Spielmann, M. and Usbeck, T.: Destructive Storms in European Forests: Past and forthcoming Impacts, European Forest Institute, 2010.

Giglio, L., Schroeder, W., and Justice, C.O.: The collection 6 MODIS active fire detection algorithm and fire products. Remote Sensing of Environment, 178, 31–41, doi:10.1016/j.rse.2016.02.054, 2016.

Gregow, H., Laaksonen, A. and Alper, M. E.: Increasing large scale windstorm damage in Western, Central and Northern European forests, 1951–2010, Scientific Reports, 7, 46397, doi:10.1038/srep46397, 2017.

Hansen, M. C., Potapov, P. V., Moore, R., Hancher, M., Turubanova, S. A., Tyukavina, A., Thau, D., Stehman, S. V., Goetz, S. J., Loveland, T. R., Kommareddy, A., Egorov, A., Chini, L., Justice, C. O. and Townshend, J. R. G.: High-Resolution Global Maps of 21st-Century Forest Cover Change, Science, 342(6160), 850–853, doi:10.1126/science.1244693, 2013.

Hardisky, M. A., Klemas, V. and Smart, R. M.: The influence of soil salinity, growth form, and leaf moisture on the spectral radiance of Spartina alterniflora canopies. Photogramm. Eng. Remote Sens., 49, 77–83. 1983.

Haylock, M, R.: European extra-tropical storm damage risk from a multi-model ensemble of dynamically-downscaled global climate models. Natural Hazards and Earth System Sciences, 11, 2847–2857, doi:10.5194/nhess-11-2847-2011, 2011.

Huo, L.-Z., Boschetti, L. and Sparks, A.M.: Object-based classification of forest disturbance types in the conterminous United States, Remote Sensing, 11(5), 477, DOI:10.3390/rs11050477, 2019.

Johns, R. H. and Hirt, W. D.: Derechos: Widespread convectively induced windstorms. Weather and Forecasting, 2, 32–49, 1987.

Kalyakin, V. N., Smirnova, O. V., Bobrovskii, M. V., Turubanova, S. A., Potapov, P. V. and Yaroshenko, A. Y.: "History of the Eastern European forest cover", in Forests of Eastern Europe, O. V. Smirnova, Ed., 151–153, Moscow, Russia, 2004. (in Russian)

Karstens, C. D., Gallus, Jr. W.A., Lee, B. D. and Finley, C.A.: Analysis of tornado-Induced tree fall using aerial photography from the Joplin, Missouri, and Tuscaloosa-Birmingham, Alabama, Tornadoes of 2011, Journal of Applied Meteorology and Climatology, 52(5), 1049–1068, doi:10.1175/JAMC-D-12-0206.1, 2013.

Kautz, M., Meddens, A. J. H., Hall, R. J. and Arneth, A.: Biotic disturbances in Northern Hemisphere forests – a synthesis of recent data, uncertainties and implications for forest monitoring and modelling, Global Ecology and Biogeography, 26(5), 533–552, doi: 10.1111/geb.12558, 2017.

Koroleva, N. V., and Ershov, D. V.: Estimation of error in determining the forest windfall disturbances area on high spatial resolution space images of LANDSAT-TM. In: Current Problems in Remote Sensing of the Earth From Space, 9, 80–86, 2012. (in Russian)

Korznikov, K. A., Kislov, D. E., Belyaeva, N. G.: The first record of catastrophic windthrow in boreal forests of South Sakhalin and the South Kurils (Russia) during October 2015 tropical cyclones, Botanica Pacifica, 8(1), 31–38, doi:10.17581/bp.2019.08115, 2019.

Köster, K., Voolma, K., Jõgiste, K., Metslaid, M. and Laarmann, D.: Assessment of tree mortality after windthrow using photo-derived data, Annales Botanici Fennici, 46(4), 291–298, doi:10.5735/085.046.0405, 2009.

Krylov, A. M., Malahova, E. G. and Vladimirova, N. A.: Identification and assessment of forest areas damaged by windfalls in 2009–2010 by means of remote sensing, Bull. Of Saint-Petersburg Academy of Forest Management, 200, 197–207, 2012. (in Russian)

Landsat Collection 1. Available from: https://www.usgs.gov/land-resources/nli/landsat/landsat-collection-1?qt-science_support_page_related_con=1#qt-science_support_page_related_con (Accessed 2 April 2020), 2019.

Lassig, R. and Moĉalov, S. A.: Frequency and characteristics of severe storms in the Urals and their influence on the development, structure and management of the boreal forests, Forest Ecology and Management, 135, 179–194, doi:10.1016/S0378 -1127(00)00309-1, 2000

Liu, Z., Peng, C., Work, T., Candau, J.-N., Desrochers, A., Kneeshaw, D.: Application of machine-learning methods in forest ecology: Recent progress and future challenges, Environmental Reviews, 26(4), 339–350. DOI:10.1139/er-2018-0034, 2018.

Los Angeles Times, 1998. 6 Die, 122 Hurt as Windy Storm Rips Up Moscow, Available from: https://www.latimes.com/archives/la-xpm-1998-jun-22-mn-62451-story.html (Accessed 3 April 2020).

Local Polynomial Interpolation – Help. ArcGIS Desktop, Available from: http://desktop.arcgis.com/en/arcmap/latest/tools/geostatistical-analyst-toolbox/local-polynomial-interpolation.htm (Accessed 3 April 2020).

Millar, C. I. and Stephenson, N. L.: Temperate forest health in an era of emerging megadisturbance, Science, 349(6250), 823–826, doi:10.1126/science.aaa9933, 2015.

Negrón-Juárez, R.I., Chambers, J.Q., Guimaraes, G., Zeng, H., Raupp, C.F.M., Marra, D.M., Ribeiro, G.H.P.M., Saatchi, S.S., Nelson, B.W., Higuchi, N., Widespread Amazon forest tree mortality from a single cross-basin squall line event. Geophysical Research Letters 37, 1–5. https://doi.org/10.1029/2010GL043733, 2010.

Nilsson, C., Stjernquist, I., Bärring, L., Schlyter, P., Jönsson, A.M., and Samuelsson, H.: Recorded storm damage in Swedish forests 1901-2000, Forest Ecology and Management, 199(1), 165–173. doi:10.1016/j.foreco.2004.07.031, 2004.

Oeser, J., Pflugmacher, D., Senf, C., Heurich, M. and Hostert, P.: Using intra-annual Landsat time series for attributing forest disturbance agents in Central Europe, Forests, 8(7), Art. No. 251, doi:10.3390/f8070251, 2017.

Overpeck, J. T., Rind, D., and Goldberg, R.: Climate-induced changes in forest disturbance and vegetation, Nature, 343(6253), 51–53, doi:10.1038/343051a0, 1990.

Pakhuchiy, V.V.: Virgin stands of coniferous taiga in the far southeastern Komi republic, Polar Geography, 21(3), 213–223. doi: 10.1080/10889379709377626, 1997.

Peterson, C. J.: Catastrophic wind damage to North American forests and the potential impact of climate change, Science of the Total Environment, 262, 287–311. doi:10.1016/S0048-9697(00)00529-5

Petukhov, I. N., and Nemchinova, A. V.: Windthrows in forests of Kostroma oblast and the neighboring lands in 1984-2011, Russian Journal of Forest Science, 6, 16–24, 2014. (in Russian)

Potapov, P. V., Turubanova, S. A., Tyukavina, A., Krylov, A. M., McCarty, J. L., Radeloff, V. C. and Hansen, M. C.: Eastern Europe's forest cover dynamics from 1985 to 2012 quantified from the full Landsat archive, Remote Sensing of Environment, 159, 28–43, doi:10.1016/j.rse.2014.11.027, 2015.

Radler, T., Groenemeijer, P., Faust, E., Sausen, R. and Púčik, T.: Frequency of severe thunderstorms across Europe expected to increase in the 21st century due to rising instability, NPJ Climate and Atmospheric Science, 30, doi:10.1038/s41612-019-0083-7, 2019.

Riemann-Campe. K., Fraedrich. K. and Lunkeit. F.: Global climatology of convective available potential energy (CAPE) and convective inhibition (CIN) in ERA-40 reanalysis, Atmospheric Research, 93, 534–545, doi:10.1016/j.atmosres.2008.09.037, 2009.

Sayn-Wittgenstein, L., and Wightman, J. M.: Landsat application in Canadian forestry. In: Proceeding of the 10th Int. Symp. on Remote Sensing of Environment, 2, 1209–1218, 1975.

Schaefer, J.T. and Edwards, R. The SPC tornado/severe thunderstorm database. In: Preprints, 11th Conf. on Applied Climatology. Amer. Meteor. Soc, Dallas, TX Available online at. https://ams.confex.com/ams/99annual/abstracts/1360.htm (6.11), 1999.

Schelhaas M. J., Nabuurs G. J., and Schuck A.: Natural disturbances in the European forests in the 19th and 20th centuries, Global Change Biology, 9(11), 1620–1633, doi:10.1046/j.1365-2486.2003.00684 .x, 2003.

Schmoeckel, J., and Kottmeier, C.: Storm damage in the Black Forest caused by the winter storm "Lothar" – Part 1: Airborne damage assessment, Natural Hazards Earth System Sciences, 8, 795–803, doi:10.5194/nhess-8-795-2008, 2008.

Seidl, R., Schelhaas, M.-J. and Lexer, M. J.: Unraveling the drivers of intensifying forest disturbance regimes in Europe, Global Change Biology, 17(9), 2842–2852, doi:10.1111/j.1365-2486.2011.02452.x, 2011.

Seidl, R., Schelhaas, M.-J., Rammer, W. and Verkerk, P. J.: Increasing forest disturbances in Europe and their impact on carbon storage, Nature Climate Change, 4(9), 806–810, doi:10.1038/nclimate2318, 2014.

Seidl, R., Thom, D., Kautz, M., Martin-Benito, D., Peltoniemi, M., Vacchiano, G., Wild, J., Ascoli, D., Petr, M., Honkaniemi, J., Lexer, M.J., Trotsiuk, V., Mairota, P., Svoboda, M., Fabrika, M., Nagel T.A. and Reyer, C. P. O.: Forest disturbances under climate change, Nature Climate Change, 7(6), 395–402. doi:10.1038/nclim ate33 03, 2017.

Senf, C., Pflugmacher, D., Zhiqiang, Y., Sebald, J., Knorn, J., Neumann, M., Hostert, P. and Seidl, R.: Canopy mortality has doubled in Europe's temperate forests over the last three decades, Nature Communications, 9(1), 4978, doi:10.1038/s41467-018-07539-6, 2018.

Shamin, S. I., Buhonova, L. K., and Sanina, A. T.: Database of hazardous and unfavourable hydrometeorological events that did damage to the economy and population of the Russian Federation. http://meteo.ru/english/climate/weather_and_hazards.php. 2019.

Skvortsova, E. B., Ulanova, N. G., and Basevich, V. F.: The ecological role of windthrow, Moscow, 1983. (in Russian)

Shikhov, A. N., and Chernokulsky, A. V.: A satellite-derived climatology of unreported tornadoes in forested regions of northeast Europe, Remote Sensing of Environment, 204, 553–567, doi:10.1016/j.rse.2017.10.002, 2018.

Shikhov, A., Chernokulsky, A., Azhigov, I., and Semakina, A.: A satellite-derived database for stand-replacing windthrow events in boreal forests of European Russia in 1986–2017. figshare. Dataset. https://doi.org/10.6084/m9.figshare.12073278.v6, 2020.

Shikhov, A. N., Chernokulsky, A. V., Sprygin, A. A., and Azhigov I. O.: Identification of mesoscale convective cloud systems with tornadoes using satellite data, Sovremennye problemy distantsionnogo zondirovaniya Zemli iz kosmosa, 16(1), 223–236, doi:10.21046/2070-7401-2019-16-1-223-236, 2019.

Shikhov, A. N., Perminova E. S., and Perminov S. I.: Satellite‐based analysis of the spatial patterns of fire and storm-related forest disturbances in the Ural region, Russia, Natural Hazards, 97, 283–308, doi:10.1007/s11069-019-03642-z), 2019.

Shikhov A. N., and Zaripov A. S.: Long-term dynamics of fire- and wind-related forest losses in northeast European Russia from satellite data, Sovremennye problemy distantsionnogo zondirovaniya Zemli iz kosmosa, 15(7), 114–128, doi:10.21046/2070-7401-2018-15-7-114-128, 2018. (in Russian)

Sun, B., Groisman, P. Y. and Mokhov I. I.: Recent Changes in Cloud-Type Frequency and Inferred Increases in Convection over the United States and the Former USSR, Journal of Climate, 14, 1864–1880, doi:10.1175/1520-0442(2001)014<1864:RCICTF>2.0.CO;2, 2001.

Suvanto, S., Henttonen, H. M., Nöjd, P., and Mäkinen, H.: Forest susceptibility to storm damage is affected by similar factors regardless of storm type: Comparison of thunder storms and autumn extra-tropical cyclones in Finland, Forest Ecology and Management, 381, 17–28, doi: 10.1016/j.foreco.2016.09.005, 2016.

Taszarek, M., Brooks, H. E., Czernecki, B., Szuster, P. and Fortuniak, K.: Climatological Aspects of Convective Parameters over Europe: A Comparison of ERA-Interim and Sounding Data, Journal of Climate, 31, 4281–4308, doi: 10.1175/JCLI-D-17-0596.1, 2018.

Taszarek, M., Pilguj, N., Orlikowski, J., Surowiecki, A., Walczakiewicz, S., Pilorz, W., Piasecki, K., Pajurek, L. and Półrolniczak, M.: Derecho evolving from a Mesocyclone-A Study of 11 August 2017 severe weather outbreak in Poland: Event analysis and high-resolution simulation, Monthly Weather Review, 147(6), 2283–2306, doi:10.1175/MWR-D-18-0330.1, 2019.

Ulanova, N.G.: The effects of windthrow on forests at different spatial scales: a review. Forest Ecology and Management 135, 155–167. doi:10.1016/S0378-1127(00)00307-8, 2000.

Usbeck, T., Waldner, P., Dobbertin, M., Ginzler, C., Hoffmann, C., Sutter, F., Steinmeier, C., Volz, R., Schneiter, G. and Rebetez, M.: Relating remotely sensed forest damage data to wind data: Storms Lothar (1999) and Vivian (1990) in Switzerland, Theoretical and Applied Climatology, 108(3-4), 451–462, doi:10.1007/s00704-011-0526-5, 2012.

Usbeck, T., Wohlgemuth, T., Dobbertin, M., Pfister, C., Bürgi, A., Rebetez, M.: Increasing storm damage to forests in Switzerland from 1858 to 2007, Agricultural and Forest Meteorology, 150(1), 47–55, doi: 10.1016/j.agrformet.2009.08.010, 2010.

van Lierop, P., Lindquist, E., Sathyapala, S., Franceschini, G.: Global forest area disturbance from fire, insect pests, diseases and severe weather events, Forest Ecology and Management, 352, 78–88, doi:10.1016/j.foreco.2015.06.010, 2015.

Wang, F., and Xu, Y. J.: Comparison of remote sensing change detection techniques for assessing hurricane damage to forests. Environmental Monitoring and Assessment, 162, 311–326, doi:10.1007%2Fs10661-009-0798-8, 2010.

Wang, W., Qu, J.J., Hao, X., Liu, Y., Stanturf, J. A.: Post-hurricane Forest damage assessment using satellite remote sensing. Agricultural and. Forest. Meteorology, 150, 122–132. doi:10.1016/j.agrformet.2009.09.009, 2010.

Westerling, A. L.: Increasing western US forest wildfire activity: Sensitivity to changes in the timing of spring, Philosophical Transactions of the Royal Society B: Biological Sciences, 371(1696), Art. No. 20150178, doi:10.1098/rstb.2015.0178, 2016.

Wulder, M. A., Masek, J. G., Cohen, W. B., Loveland, T. R., and Woodcock, C. E.: Opening the archive: how free data has enabled the science and monitoring promise of Landsat, Remote Sensing of Environment, 122, 2–10, doi:10.1016/j.rse.2012.01.010, 2012.

WWF Russia's Boreal Forests. Forest Area Key Facts & Carbon Emissions from Deforestation, Available from: http://assets.panda.org/downloads/russia_forest_cc_final_13nov07.pdf (Accessed 3 April 2020).

Ye, H., Fetzer E. J., Wong. S., and Lambrigtsen B. H.: Rapid decadal convective precipitation increase over Eurasia during the last three decades of the 20th century, Science Advances, 3, e1600944, doi: 10.1126/sciadv.1600944, 2017.

Field name	Field alias	Type, length	Description
OBJECTID	OBJECTID	Object ID	Index number of EDA
ID	Windthrow ID	Short	Windthrow ID
Storm_ID	ID of storm event	Short	ID of a storm event
Area	Area (km^2)	Float	EDA area (km^2)

870 **Table 1: Attribute table of the GIS layer of elementary damaged areas (EDAs).**

Field name	Field alias	Type, length	Description
OBJECTID	OBJECTID	Object ID	Index number of windthrow
ID	Windthrow ID	Short	A windthrow ID
Storm_ID	ID of storm event	Short	ID of storm event
Storm_type	Type of storm	String, 10	A type of a storm that caused the windthrow: convective windstorm, tornado, non-convective windstorm, or snowstorm
Certainty	Event certainty degree	String, 20	The degree of certainty of storm type determination: high or medium
Source_1	Data source for windthrow delineation	String, 50	Data source for windthrow delineation
Source_2	Data source for windthrow type defining	String, 100	Data source for windthrow type defining
Year	Year	Short integer	The year of the windthrow event
Month	Month	Short integer	The month of the windthrow event
Date	Storm event date	String, 20	The date of storm event
Date_1	Date of first image	Date	The date of the last Landsat/Sentinel-2 image that lack the windthrow
Date_2	Date of second image	Date	The date of the first Landsat/Sentinel-2 image, by which the windthrow was detected
Time_range	Time range	String, 50	Time range of storm event (UTC)
Time_Src	Data source for determine storm time range	String, 255	Data source or URL that was used to determine the time range of a storm event
N_polygons	Number of single-part polygons	Short	Number of single-part polygons
Area	Area (km^2)	Float	Windthrow area (km^2)
Length	Path length (km)	Float	Length of windthrow (km)
Mean_width	Mean width of windthrow excluding gaps (m)	Float	Mean width of windthrow (m) — for damaged area only
Max_width	Max width of windthrow excluding gaps (m)	Float	Maximum width of windthrow (m) —for damaged area only
Mean_w_2	Mean width of windthrow with gaps (m)	Float	Mean width of windthrow including gaps (m)
Max_w_2	Max width of windthrow with gaps (m)	Float	Maximum width of windthrow including gaps (m)
Direction	Direction of windthrow	String, 10	Elongated direction of windthrow, i.e. direction of storm movement
Near_WS	WMO ID of the weather station	Long	WMO ID of the nearest weather station — if the distance between windthrow and weather station is less than 50 km or weather station located on the storm track
WS_dist	Distance to weather station	Float	Distance to the nearest weather station (km)

	(km)		
Wind_gust	Wind gust (m/s)	Short	Maximum wind gust that measured by the weather station on a day when windthrow occurred
Gust_time	Wind gust time (UTC)	Short	Time of wind gust report (UTC) with 3-hour accuracy
Sum_prec	Precipitation amount	Short	Precipitation amount (only for events with heavy rainfall ≥ 30 mm/12h)
WS_comment	Additional data from weather station	String, 100	Additional data on the storm event reported by the weather station, i.e. heavy rainfall (≥ 30 mm/12h), large hail, tornado
URL	External URL	String, 100	URL of the additional data source (newspaper report or video)

875

Table 2: Attribute table of the GIS layer of windthrow areas in the forest zone of the ER (1986-2017).

Field name	Field alias	Type, length	Description
OBJECTID	OBJECTID	Object ID	Index number of a storm track
Storm_ID	ID of storm event	Short	ID of a storm event
Count	Number of windthtows	Short	Number of windthrow caused by a storm event
Area_tr	Area (km^2)	Float	Total damaged area (km^2)
Length_tr	Path length (km)	Float	Total path length with gaps, km)
Mean_w_tr	Mean width of storm track (m)	Float	Mean width of storm track (km)
Max_w_tr	Max width of storm track (m)	Float	Maximum width of storm track (km)

Table 3: Attribute table of the GIS layer of storm events tracks.

Degree of certainty	Windthrow induced by		
	Tornado	**Convective storm**	**Non-convective storm**
High (>95% likelihood of occurrence)	Independent confirmation of the tornado event (photo, video, etc.); well-detected rotation of the fallen trees (counterclockwise usually); all three additional signatures are confirmed (in the lack of the HRI)	Elongated, but amorphous (mosaic) spatial structure of forest disturbances and a varying degree of forest damage; the direction of the fallen trees generally corresponds to a storm track direction	Independent confirmation of non-convective storm causing windthrow by weather station or/and eye-witness/newspaper report;
Medium (50–95% likelihood)	The HRI are unavailable or do not allow to determine the direction of the fallen trees and only two out of three additional signature are confirmed.	HRI are unavailable or do not allow to determine the direction of the fallen trees; quasi-linear structure of a windthrow without turns of a track, and a ratio of length and width < 10:1	The date of a storm event indicate a low probability of a convective storm (e.g., autumn season) and lack of elongation along the wind direction (especially for windthrow induced by snowstorms)

Table 4: The signatures used to assess the degree of certainty of windthrow type determination.

885

Number	Total area (GFC/HRI), km^2	*A* (overlapped), km^2	Producer's accuracy, %	User's accuracy, %	*L*, km (GFC/HRI)	W_{mean}, m (GFC/HRI)	W_{max}, m (GFC/HRI)
1	6.08/6.49	5.04	77.6	82.8	9.4/9.4	588/612	1433/1467
2	4.36/5.11	2.98	58.5	68.5	15.9/17.2	290/405	860/1798
3	1.74/1.54	0.75	48.7	43.2	42.5/42.5	104/87	542/390
4	1.55/1.31	0.79	60.3	51.3	9.0/9.1	178/152	681/593
5	1.33/0.92	0.71	77.0	53.6	6.7/6.8	220/145	638/510
6	1.00/0.76	0.41	53.9	41.1	21.8/21.8	86/70	343/250
7	0.88/0.76	0.41	53.9	46.6	14.6/14.7	112/97	458/382
8	0.42/0.32	0.19	59.7	44.5	7.4/7.2	85/53	233/179
9	0.27/0.14	0.11	77.2	41.7	2.1/2.1	136/79	306/264
10	0.26/0.25	0.15	61.4	60.0	9.4/9.4	86/59	188/206

Table 5: Comparison of windthrow geometrical parameters estimated using the GFC and HRI data.

Number	A, km^2 (EEFCC/HRI),	A (overlapped), km^2	Producer's accuracy	User's accuracy	L, km (EEFCC/HRI)	W_{mean}, m (EEFCC/HRI)	W_{max}, m (EEFCC/HRI)
1	3.11/4.18	2.58	82.96	61.72	14.6/14.2	308/257	963/748
2	1.59/2.35	1.25	78.62	53.19	16.8/16.9	186/148	568/491
3	3.48/3.82	2.68	77.01	70.16	14.2/14.9	305/288	1507/1269
4	0.82/1.11	0.67	81.71	60.36	10.3/10.4	166/158	367/332
5	1.09/1.28	0.94	86.24	73.44	9.5/10.1	171/161	380/291

Table 6: Comparison of windthrow geometrical parameters estimated using the EEFCC and HRI data.

Windthrow type	Degree of certainty	Number of windthrow	Damaged area, km^2
Convective storm induced	High	270	2371.6
	Medium	25	7.6
Tornado-induced	High	295	300.4
	Medium	92	79.2
Non-convective storm induced	High	12	131.8
	Medium	6	5.9
Total	High	577	2803.8
	Medium	123	92.7

Table 7: Total number of windthrow events of different types and corresponding forest damaged area.

895

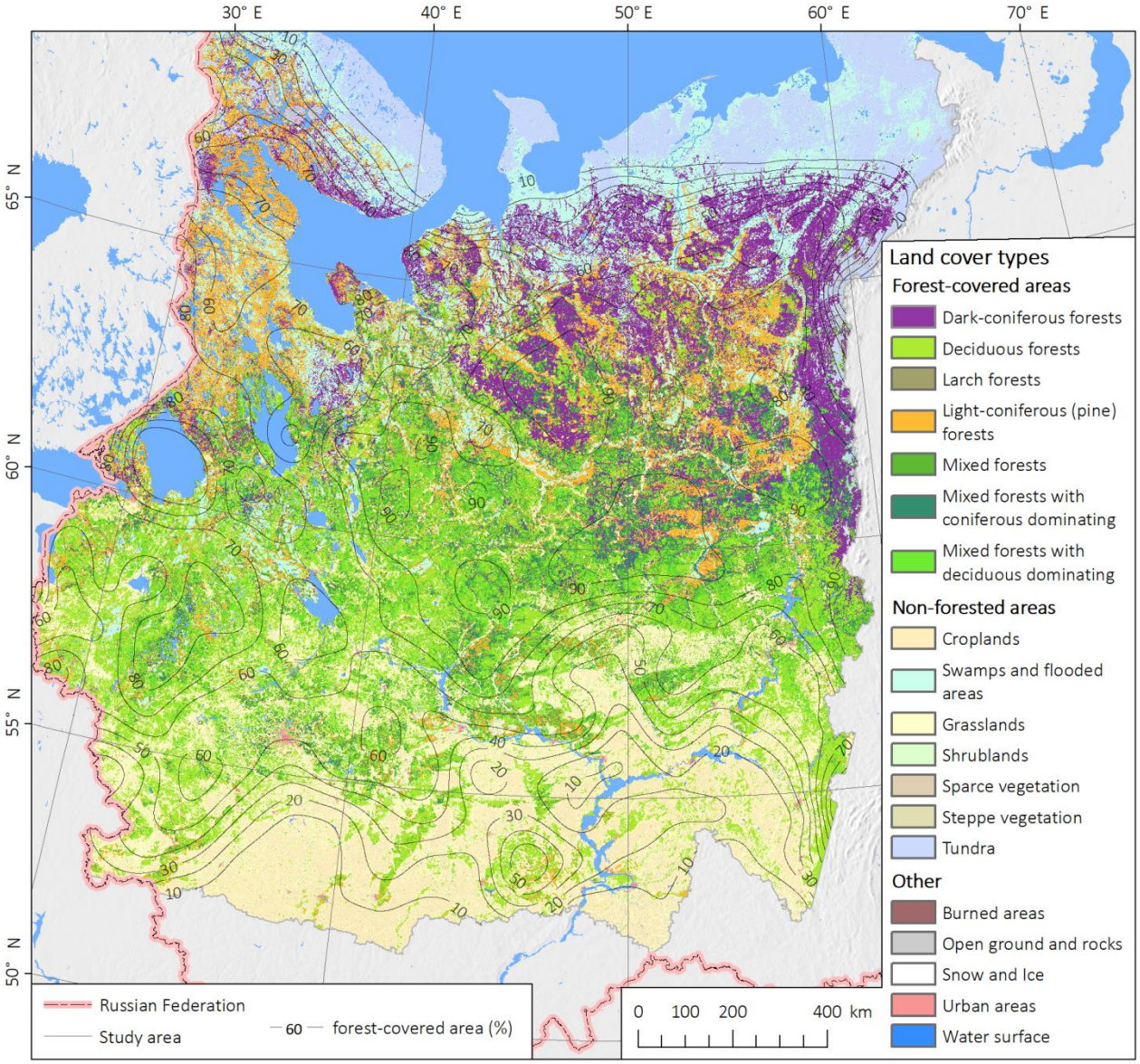

Figure 1: Land cover types within the study area, according to the map of vegetation cover of Russia, developed by the Space Research Institute of the Russian Academy of Sciences (Bartalev et al., 2016).

900

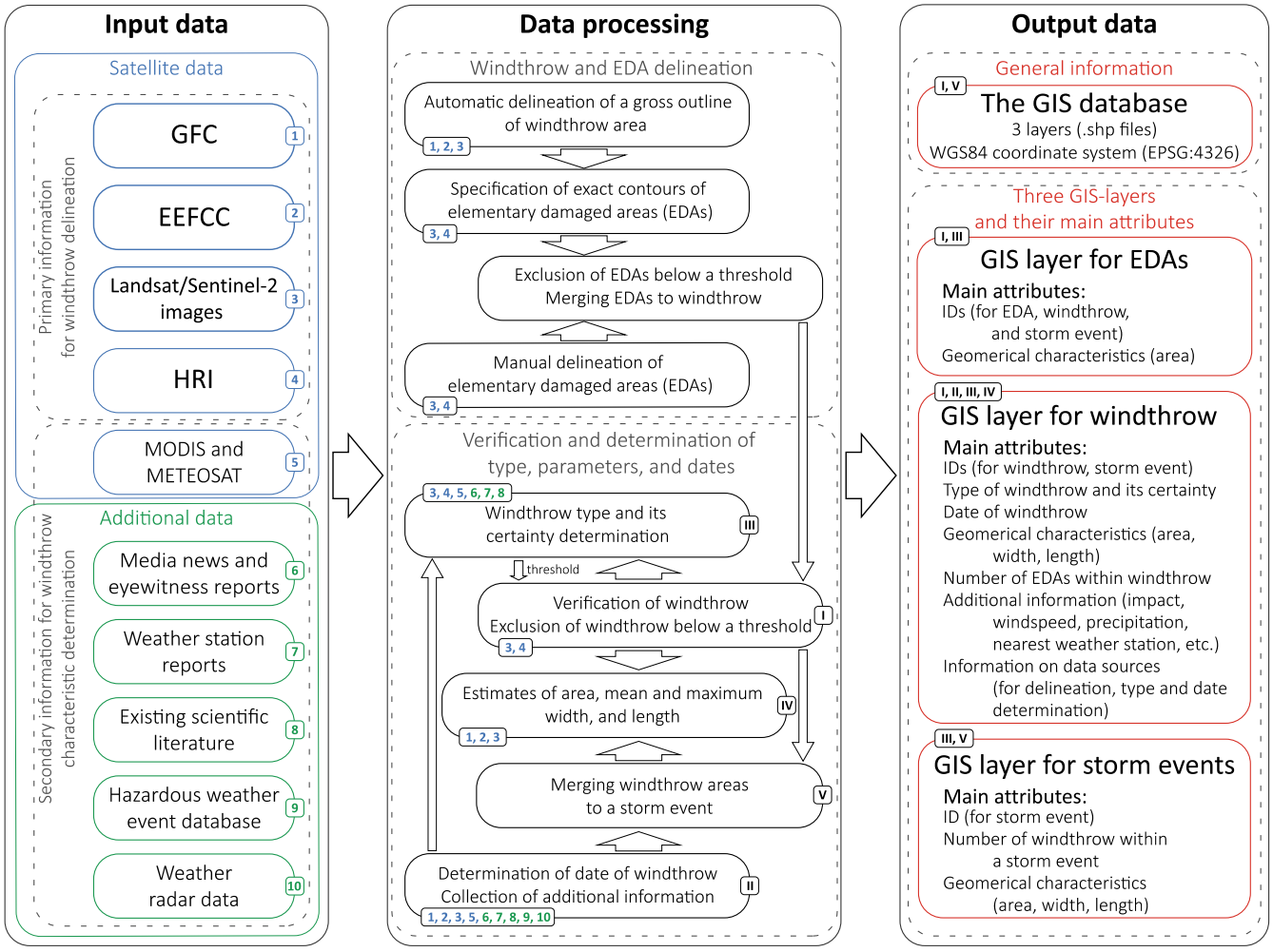

Figure 2: The workflow used for windthrow delineation and attribution.

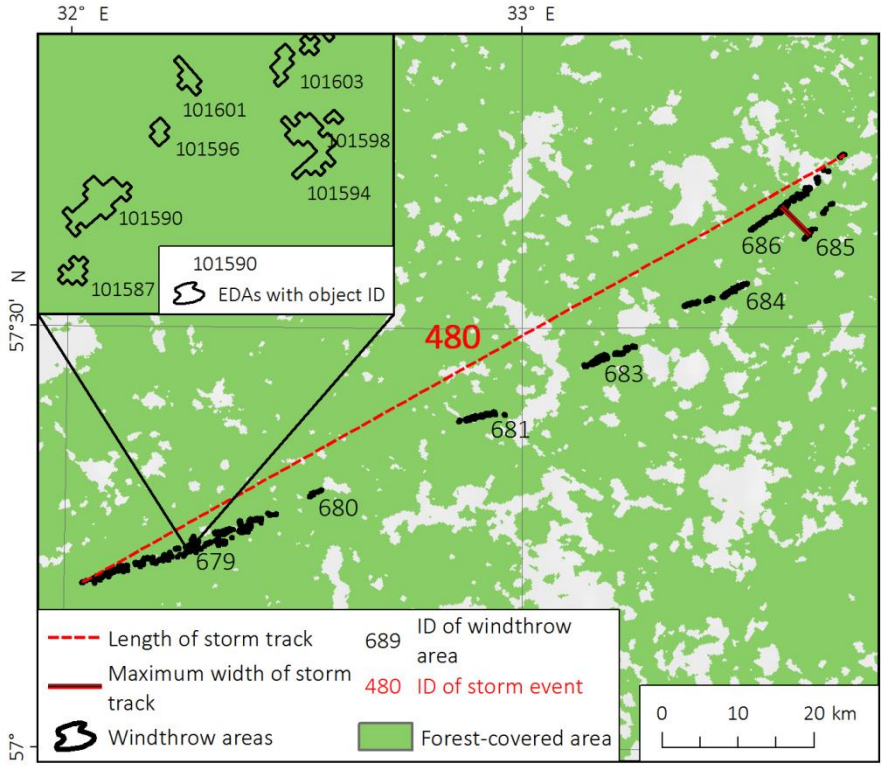

905 **Figure 3: An example of three hierarchical levels of the database** for the event occurred on 2 Aug 2017. A scheme for the determination of geometrical parameters of a storm event is also shown. Parallel (680, 681) and successive (684, 689, 682, 678) locations of windthrow areas are indicated as well.

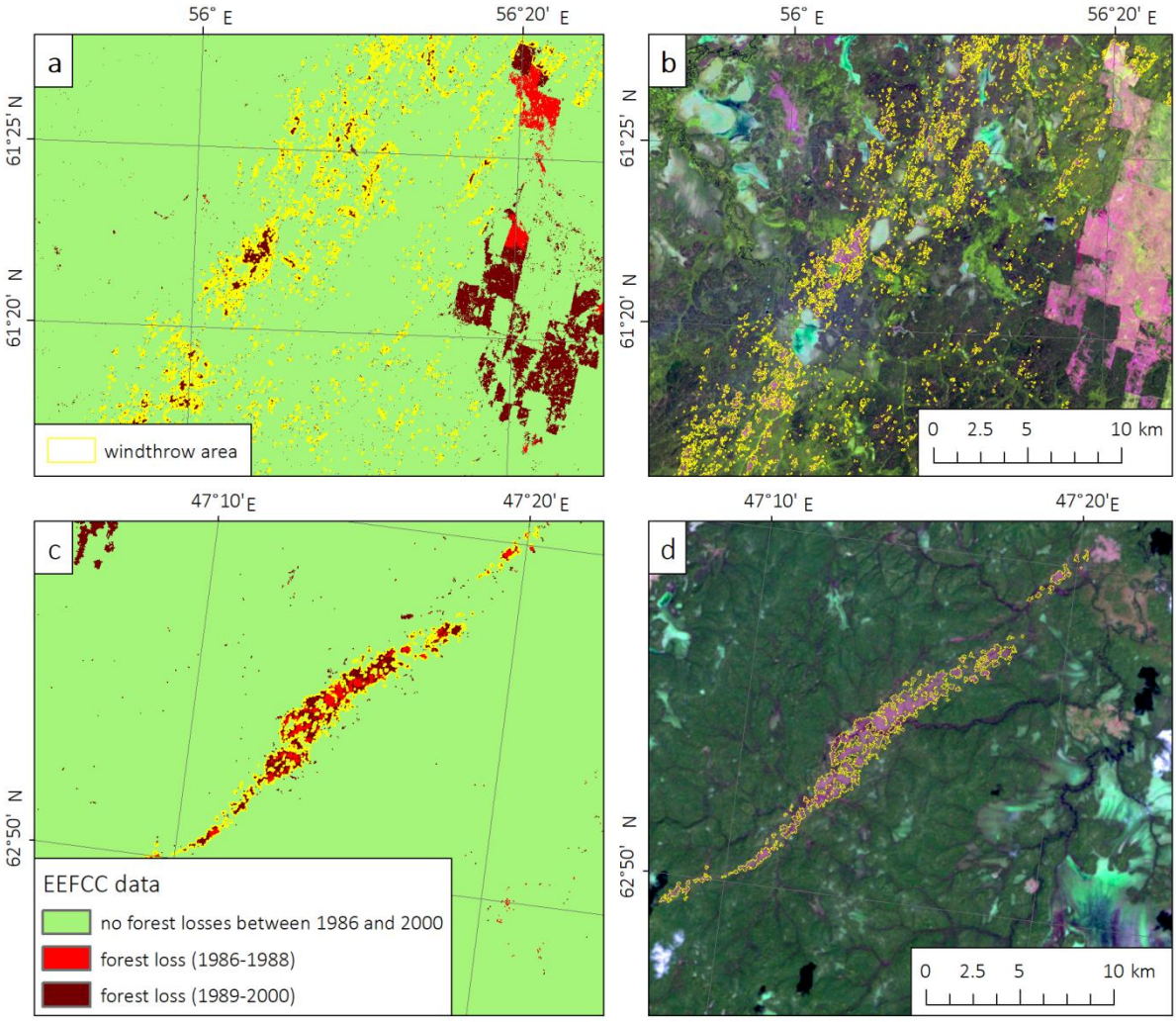

910

Figure 4: Delineation of (a, b) storm- and (c, d) tornado-induced windthrow occurred on 4 July 1992 and 24 July 1988 respectively based on (a, c) the EEFCC dataset and (b, d) its subsequent verification by the Landsat images, shown in the RGB combination of the TM5 (1.65 μm), TM4 (0.85 μm), and TM3 (0.66 μm) spectral bands.

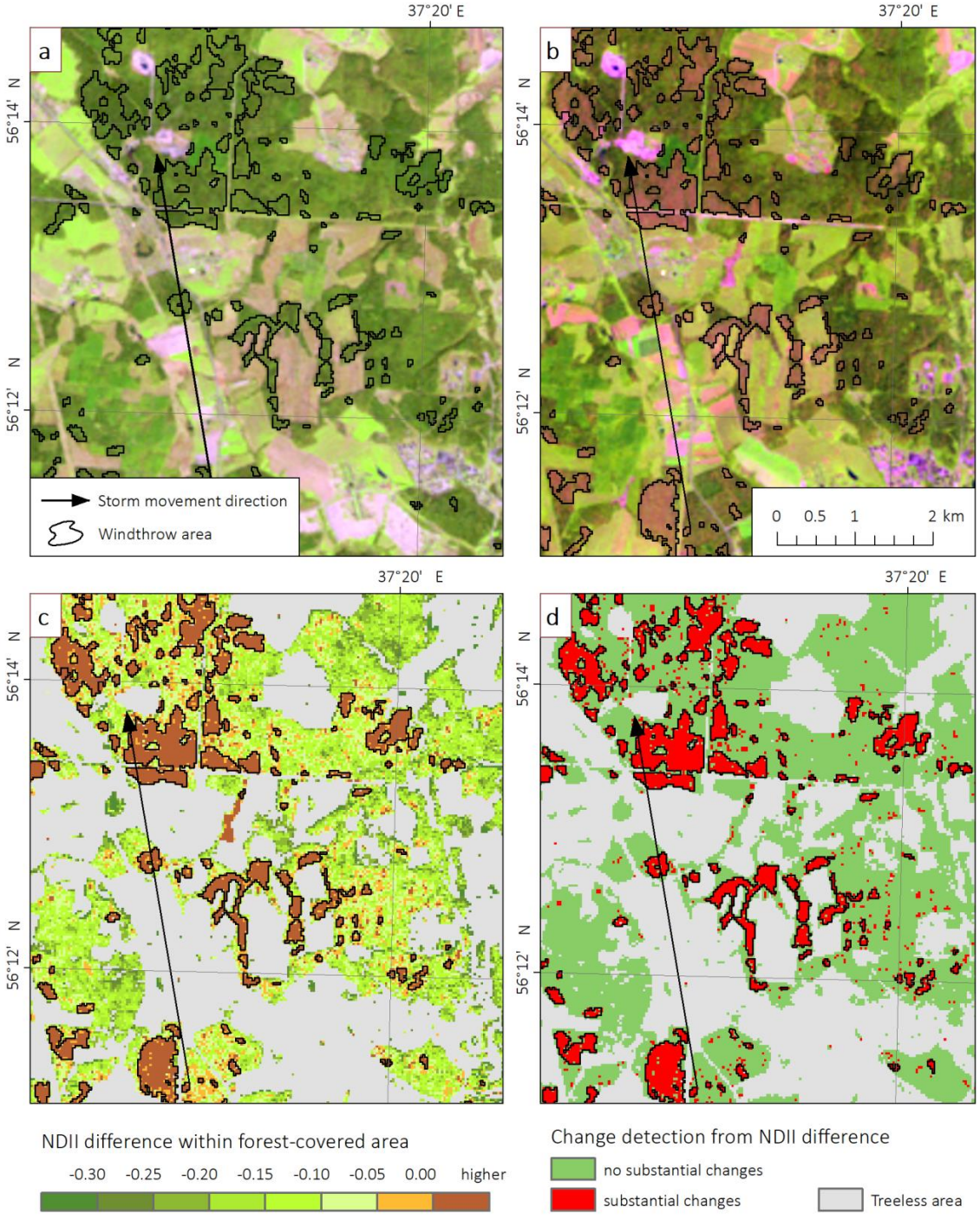

915

Figure 5: Delineation of windthrow caused by the windstorm that occurred on 21 June 1998 in Moscow region based on the NDII difference method: the Landsat-5 images obtained (a) before and (b) after the storm event — 11 May 1998 and 30 July 1998, respectively; (c) the NDII difference within forest-covered area and (d) the areas with the substantial decrease of the NDII.

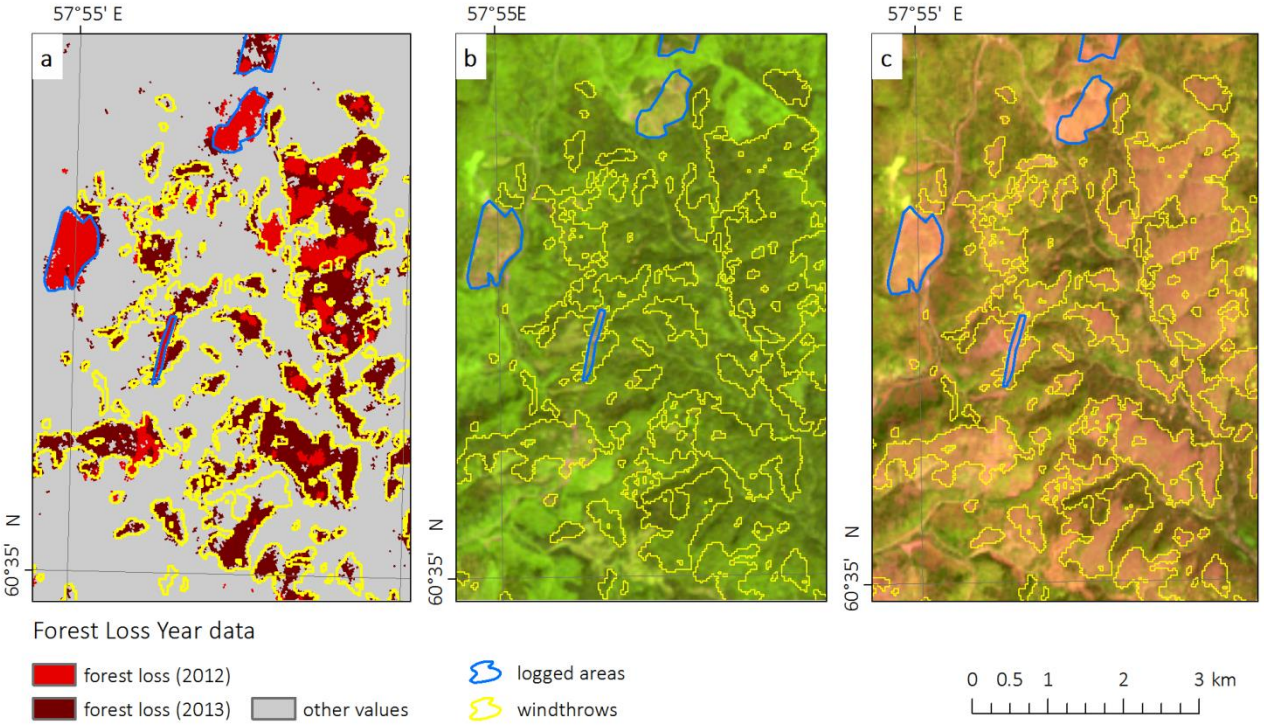

920

Figure 6: Separation of the windthrow occurred on 18 July 2012 from logged areas based on (a) the GFC data on forest losses, and the Landsat images obtained (b) before (i.e., 8 July 2012) and (c) after (i.e., 18 Aug 2012) the storm event.

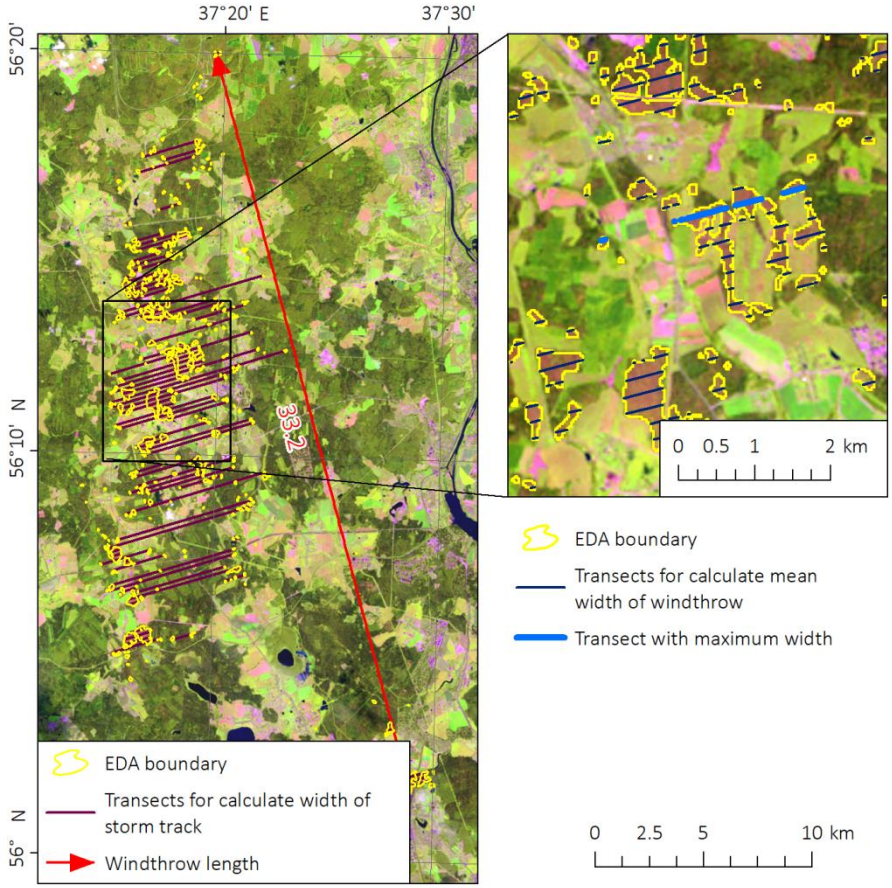

925

Figure 7: A scheme for the determination of geometrical parameters of a windthrow based on the Landsat image using the example of the windthrow in the Moscow region occurred on 21 June 1998.

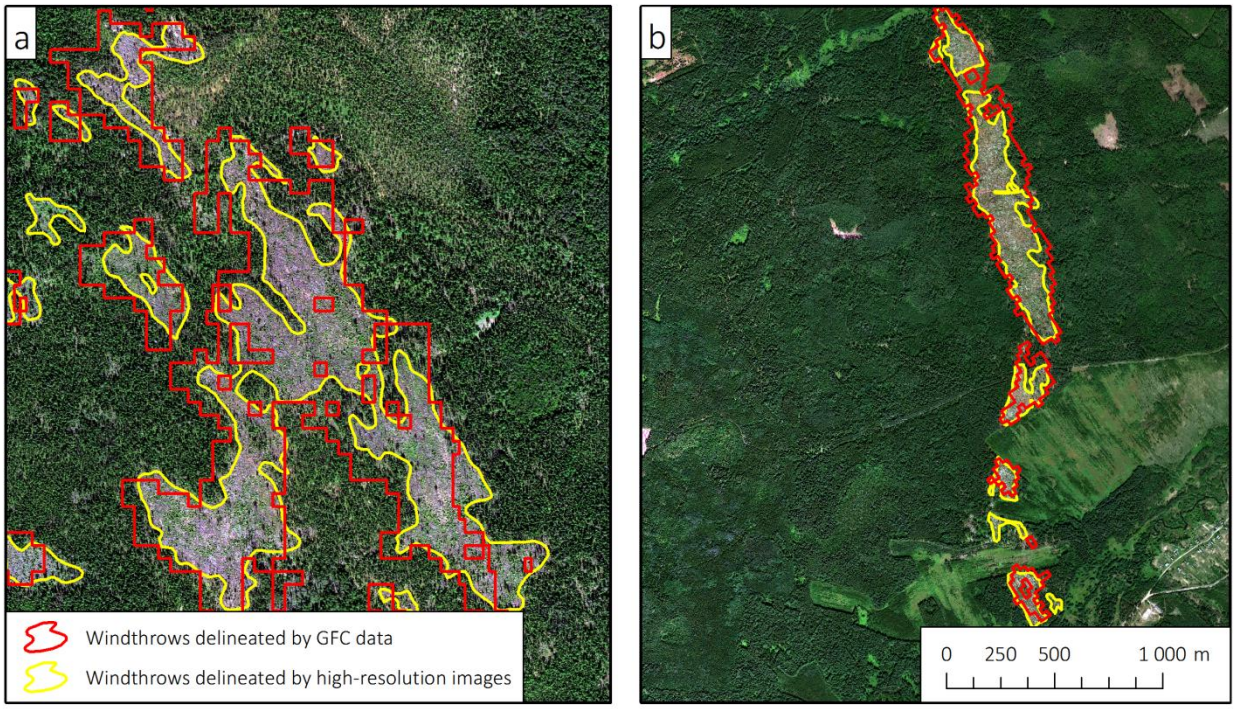

Figure 8: Overlapping of windthrow areas that extracted from the GFC dataset and delineated manually using the HRI for (a) convective-storm induced windthrow (18 July 2012), and (b) tornado-induced windthrow (June 2011).

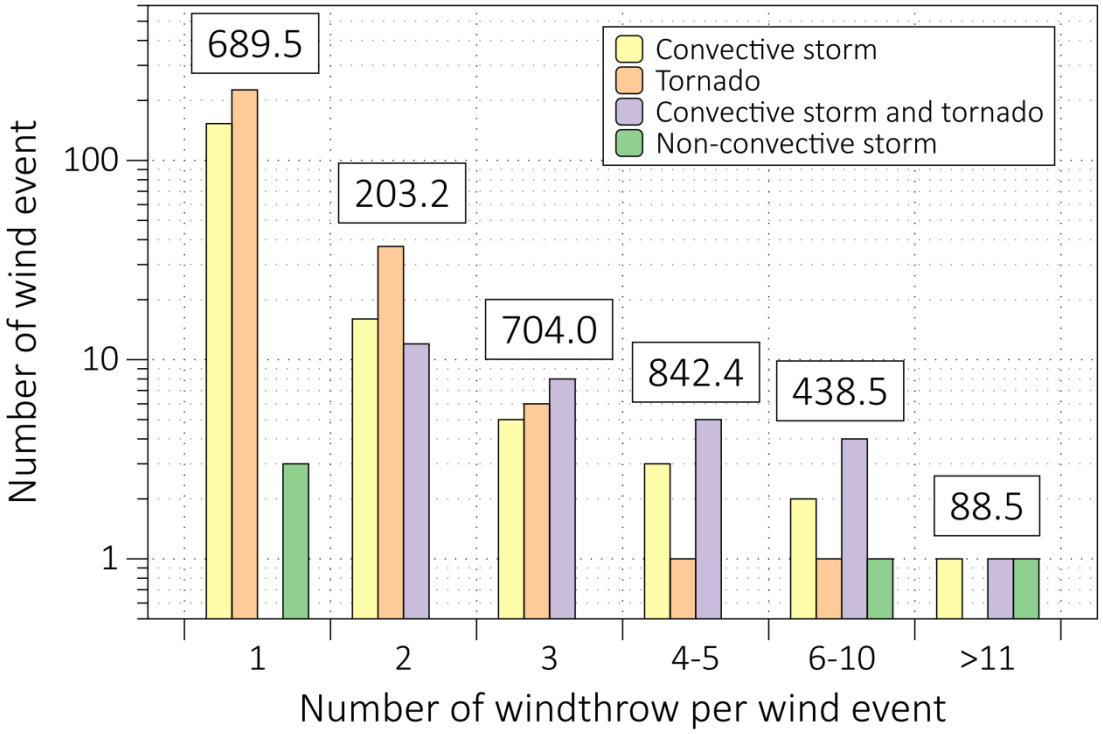

935

Figure 9: Number of windthrow per one storm event. Total damaged area (in km^2) corresponding to all type of windthrow is shown in box for each category.

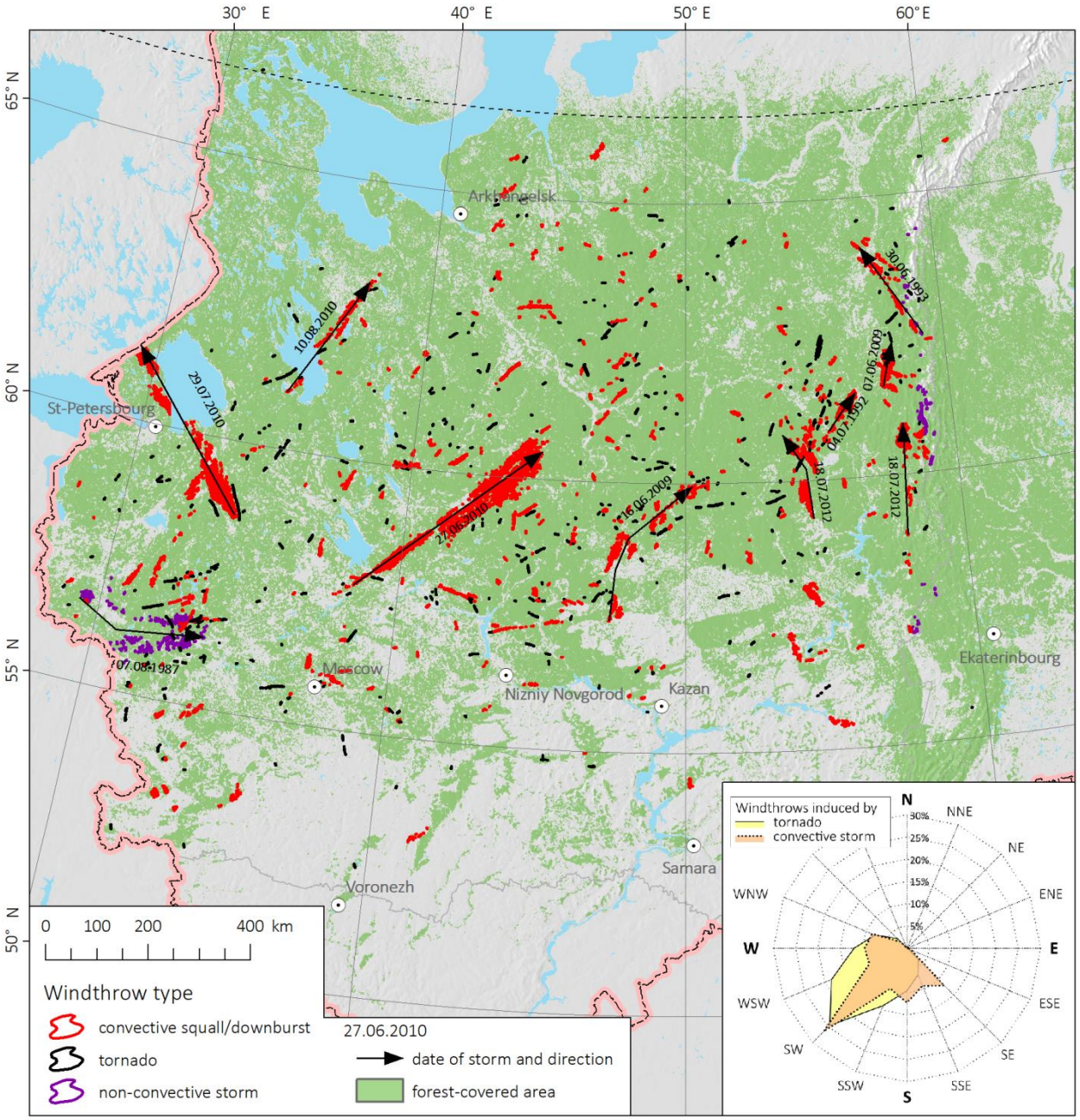

940 **Figure 10: Spatial distribution of stand-replacing windthrow in the ER in 1986-2017.** The ten most catastrophic windthrow with the largest damaged area are shown by arrows and indicated by the corresponding dates of windthrow. Forest-covered area is estimated according to the data from Bartalev et al. (2016). The inset show the direction from which windthrow originate.

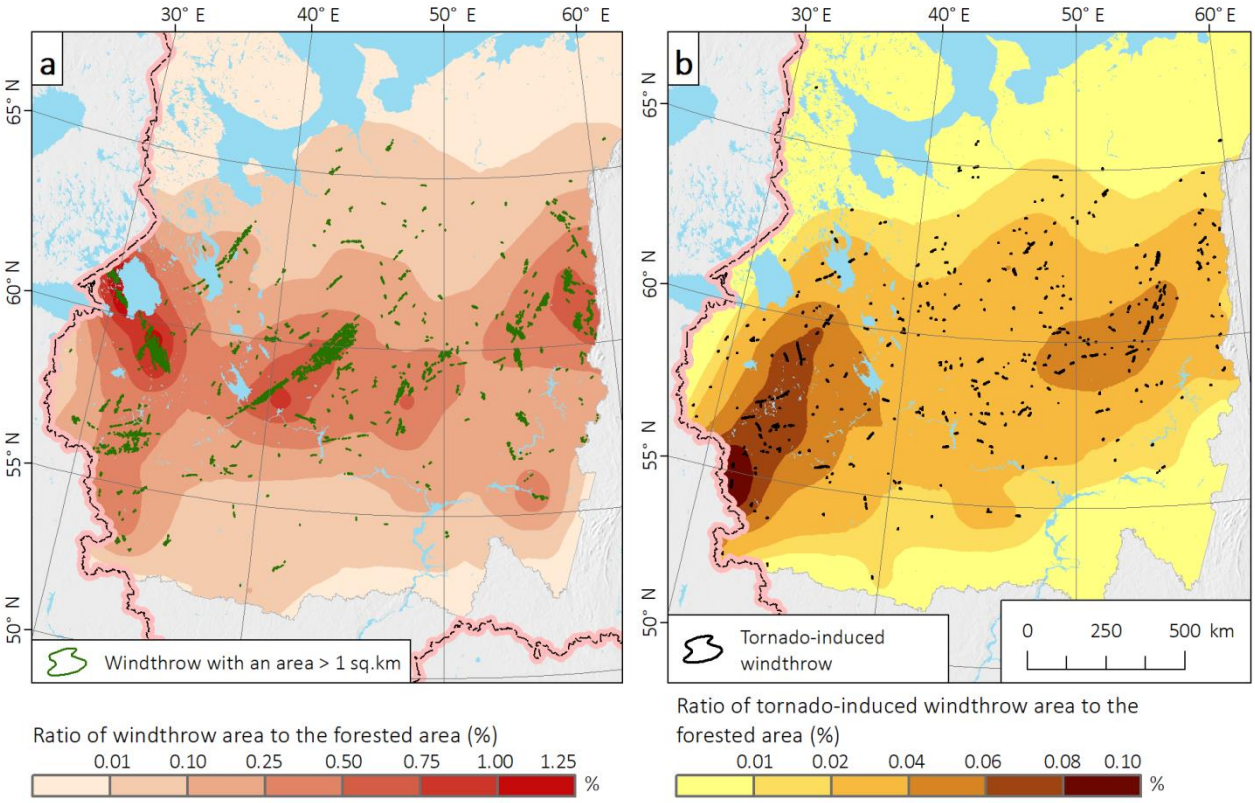

945 **Figure 11: Ratio of damaged area to the forest-covered area for (a) all windthrow and (b) tornado-induced windthrow only.** The ratio of windthrow area to the forest-covered area was calculated for 100 km^2 cell and then interpolated with local polynomial interpolation method in the ArcGis Geostatistical Analyst.

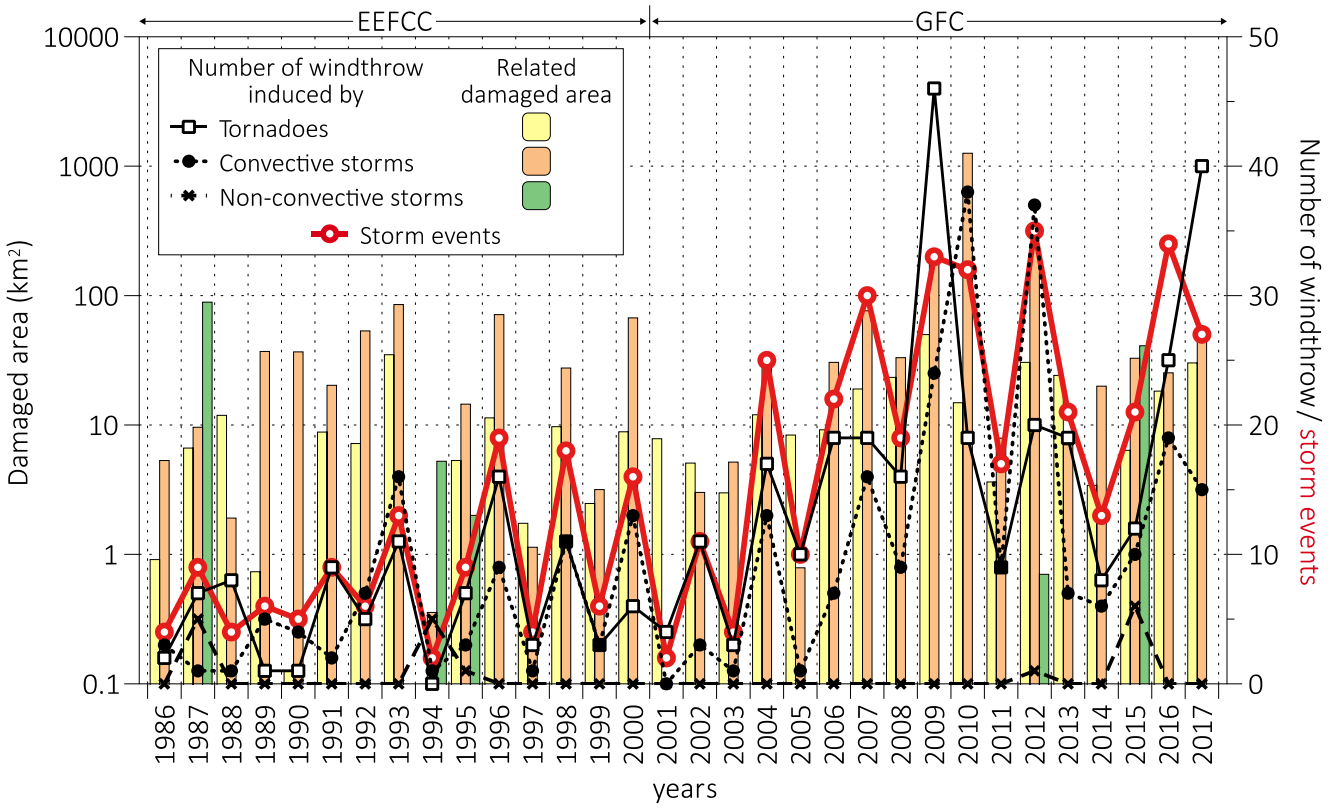

Figure 12: Interannual variability of the number of windthrow, related damaged area, and number of storm events. Note the logarithmic scale for the damaged area. Periods for the EEFCC and GFC datasets are indicated.

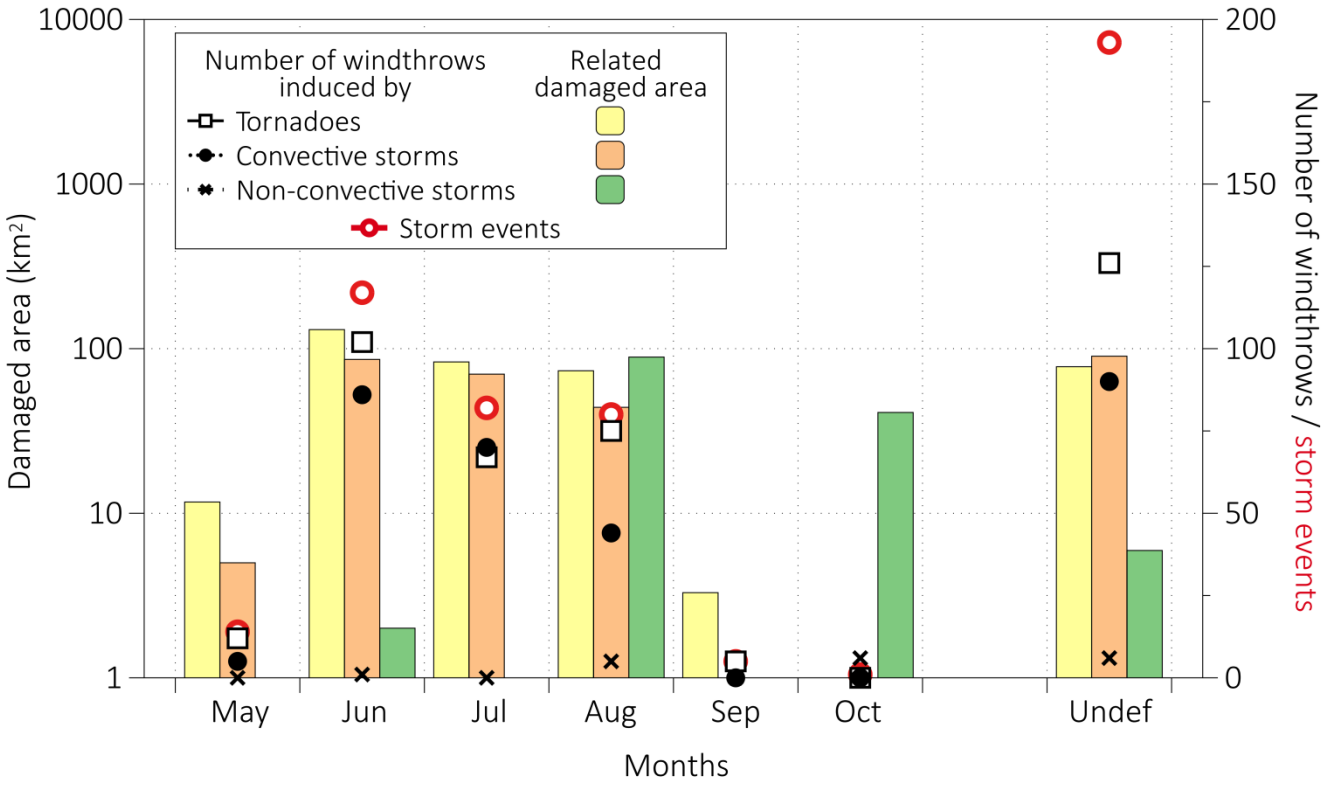

955 **Figure 13: Annual cycle of the number of windthrow, related damaged area, and number of storm events.** Note the logarithmic scale for damaged area.

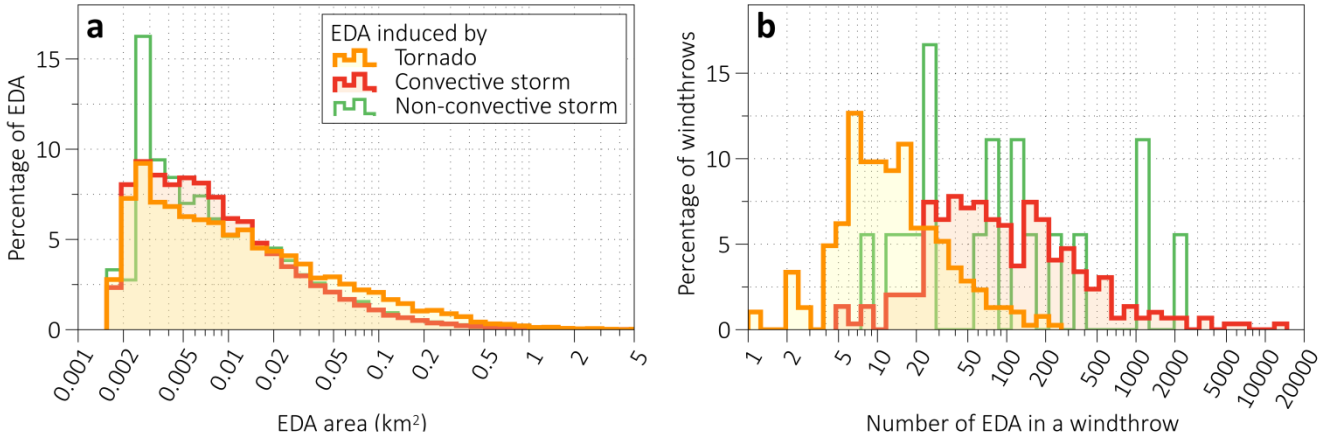

Figure 14: Distribution of (a) size of EDAs for different types of windthrow and of (b) a number of EDAs within one windthrow.

960

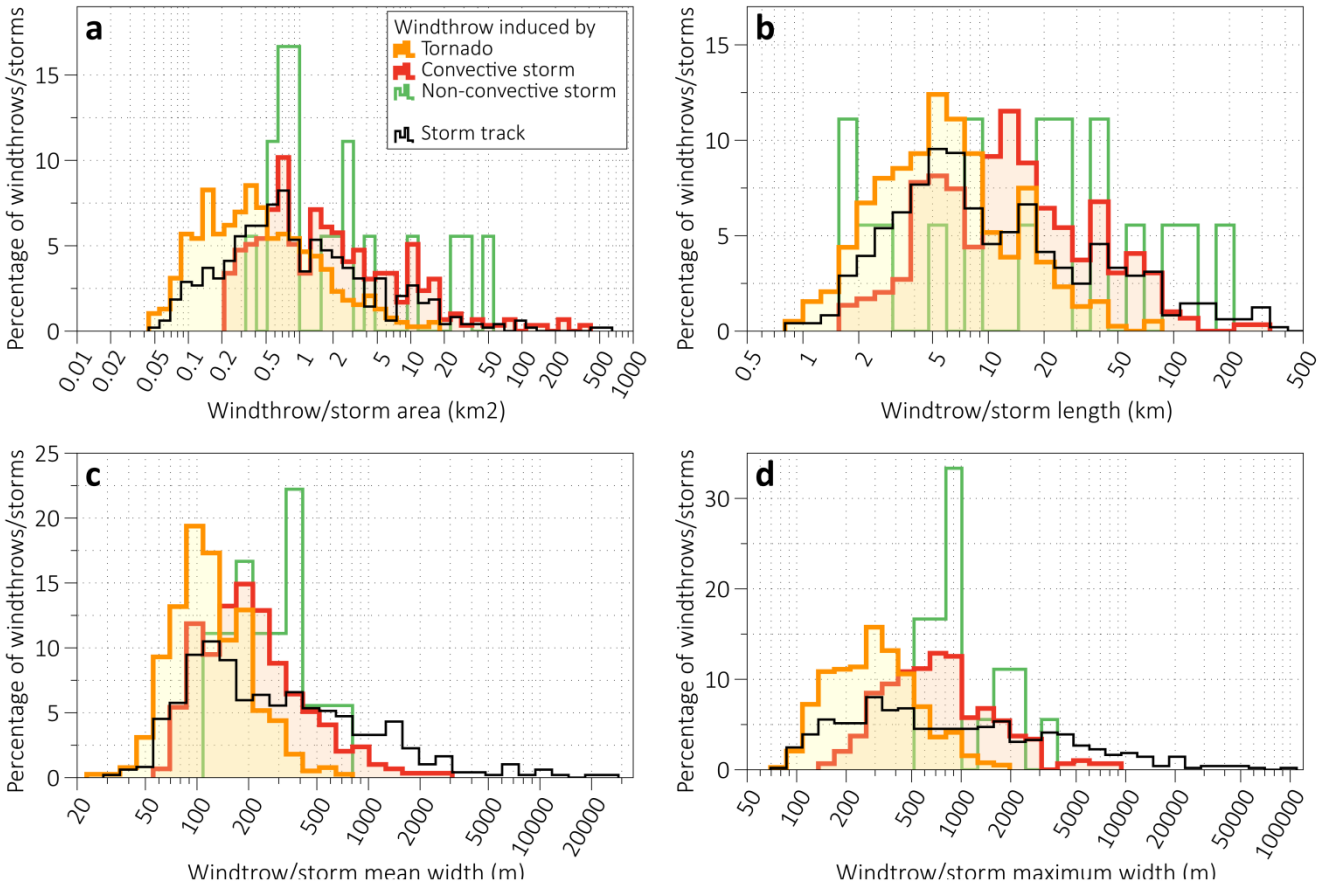

Figure 15: Distribution of geometric parameters of windthrow of different types and storm tracks: (a) area, (b) length, (c) mean width, and (d) maximum width.

965